TIDES IN THE WEDDELL SEA

Robin Robertson, Laurie Padman†, and Gary D. Egbert

College of Oceanic and Atmospheric Sciences
Oregon State University
Corvallis, Oregon
† *Now at Earth and Space Research*
Seattle, Washington

We use a high-resolution barotropic tidal model to predict tidal elevations and currents in the Weddell Sea. The ocean cavity under the Filchner-Ronne Ice Shelf is included in the model domain. Tidal elevations exceed 1 m at the back of the Filchner-Ronne and Larsen Ice Shelves. Tidal velocities are small over the deep basins but are generally greater than 10 cm s^{-1} over the continental shelves. Velocities occasionally reach 1 m s^{-1} in the shallow water near the General Belgrano Bank and under the Ronne Ice Shelf near the ice front. Model performance was evaluated through comparisons with TOPEX/Poseidon altimetry, bottom pressure gauge records, and current meter data. The largest discrepancies between the model results and measurements occur over the continental slope and under the ice shelves. The principal error sources are believed to be inaccurate bathymetry in our model, tidal analysis limitations associated with short data record lengths, and omission of baroclinic tides. Model results indicate that tides play a significant role in the circulation and heat flux in the Weddell Sea. We discuss the influence of tides on mean flow through the modified effective bottom drag, and the generation of baroclinic tides and other internal gravity waves through interactions of the tide with topography.

1. INTRODUCTION

Recent studies have greatly improved our understanding of the ways in which tides can influence lower-frequency ocean variability [e.g., *Hatayama et al*., 1996; *Ffield and Gordon*, 1996]. These authors focused on the potential for added vertical mixing in the pycnocline caused by shear instabilities initiated by baroclinic tides and other internal gravity waves, that can be generated when barotropic tides encounter steep or rough topography. This mixing can modify sea surface temperatures and salinities and, where the spatial gradient in the pycnocline mixing rate is large, generate geostrophically-balanced flows. Tidal current interactions with topography can also cause "rectified mean flows" [*Robinson*, 1981], which are Lagrangian circulations that may be an important component of net advective transport in some regions [e.g., *Loder*, 1980; *Kowalik and Proshutinsky*, 1995].

Studies of tides in high-latitude seas confirm these general influences discussed above. For example, *Polyakov* [1995] used a baroclinic tidal model to demonstrate that mixing associated with tidal currents near the basin boundaries can explain much of the spatial structure of the salinity field in the Arctic. *Parsons* [1995] found, using a three-dimensional model that included both tides and wind forcing, that the hydrographic field over the shallow shelf seas of the eastern Arctic is significantly modified by the addition of the tide. When the response of sea ice to the underlying oceanic tidal field is also considered, the influence of tides in the Arctic becomes even more profound. Tidal-frequency shear and strain fracture the sea ice, while open-water formation by periodic ice divergence greatly increases the mean loss of heat from the ocean to the polar atmosphere, with a subsequent increase in upper-ocean salinity as additional ice forms in the leads [*Kowalik and Proshutinsky*, 1994].

The present study explores the possibility that, as in the Arctic, tides in the Weddell Sea affect the lower-frequency oceanographic variability of the region. The Weddell Sea is an important element of the global "conveyor belt" [*Broecker and Peng*, 1982], being responsible for much (perhaps 50%) of the world ocean's Antarctic Bottom Water (AABW) production [e.g., *Carmack*, 1977]. For at least a decade, tides have been suspected of aiding this production, which involves the formation and mixing of distinct water types including cold, saline Western Shelf Water (WSW) and Warm Deep Water (WDW). *Foster et al.* [1987] suggested that mixing of WSW and WDW at the shelf/slope front is increased by energetic baroclinic tides and internal waves on the upper slope. *Foldvik and Gammelsrød* [1988] noted that the formation of high-salinity WSW was enhanced by increased open water near the Ronne ice front due, in part, to tidal divergence. *Levine et al.* [1997] suggested that the properties of the dense plume that flows off the shelves to become Weddell Sea Deep and Bottom Water and, ultimately AABW, will be modified by the increased benthic stirring due to tides. Increases in mean benthic stress due to tides might also retard the general oceanic circulation, which in this region consists of the wind- and thermohaline-forced Weddell Gyre.

Several measurements of tidal elevations and velocities have been made in the Weddell Sea [e.g., *Lutjeharms et al*., 1985; *Pedley et al*., 1986; *Foldvik et al*., 1990; *Levine et al*., 1997], but their spatial coverage is far from complete. Data are particularly sparse over the continental shelf and slope of the southwestern Weddell Sea, where much of the water mass formation and mixing responsible for AABW production is expected to occur. Numerical models provide the most effective method for improving our knowledge of tides in this region. The tides under the Filchner-Ronne Ice Shelves (FRIS) have been modeled by *Smithson et al.* [1996]; however, much of the Weddell Sea and the entire Scotia Sea were excluded from their domain. We have, therefore, constructed a high-resolution, non-linear, finite-difference, barotropic tidal model of the Weddell and Scotia Seas. The model is described in section 2, and available tidal measurements are reviewed in section 3. Output tidal fields are described in section 4. Model performance is evaluated with respect to observations, and the output from three global tidal models. The tidal energy budget is described in section 5. In section 6, we review two mechanisms by which tides might modify the Weddell Sea circulation and hydrographic structure: the reduction of the mean flow by the increase in the effective bottom friction; and generation of baroclinic tides. The influence of tides on the sea-ice cover is addressed in a separate paper [*Padman et al*., 1998]. A summary, including ideas for future work, is provided in section 7.

2. MODELING APPROACH

2.1. *Model Domain, Bathymetry, and Grid*

Our model domain extends from 83°10'S to 55°00'S, and from 84°00'W to 10°00'E (**Figure 1**). This region includes the ocean cavity under the FRIS, and other ice shelves. Over most of the domain, we

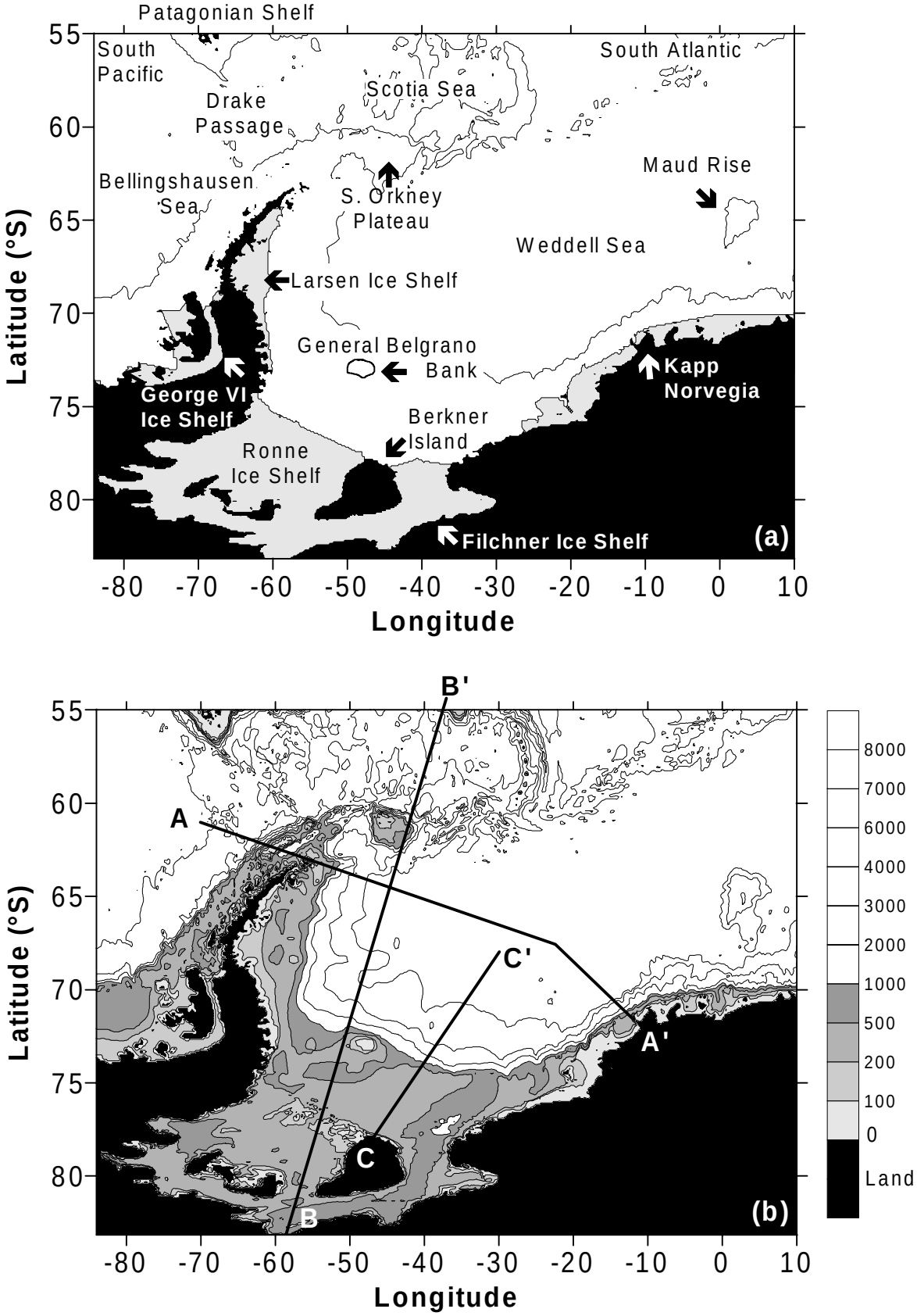

Fig. 1. (a) The model domain with topographic features noted. Ice shelves are shaded gray and the 3000 m isobath is indicated. (b) Water column height over the model domain, which is water column thickness under the FRIS and bathymetry elsewhere. Depths less than 1000 m are shaded, and the other contours that are shown are indicated on the scale. The locations of three transects, A-A', B-B', and C-C' (see Figure 3), are shown.

obtained bathymetry from the ETOPO-5 database, which provides depths on a 1/12° global grid [*National Geophysical Data Center*, 1992]. However, modifications to the model bathymetry were made in several regions where more recent data have become available. Bathymetry based on satellite altimetry and aircraft gravimetric surveys, as well as depth measurements from Ice Station Weddell [*LaBrecque and Ghidella*, 1993] was used in the western Weddell Sea in the region 73°S to 65°S, and 60°W to 44°W. Minor additional modifications were made along the edges of this region to smooth the transition between the two data sets. Under the FRIS, measurements of water column thickness were used instead of bathymetry [*Vaughan et al.*, 1994]. Bathymetry in front of the FRIS was modified to agree with *Gammelsrød et al*. [1994]. Throughout the domain, depths less than 2 m have been converted to land to avoid the occurrence of negative water column thickness, which can otherwise result as tidal elevation fluctuates.

An Arakawa-C grid was used. The grid spacing is 1/6° in longitude and 1/12° in latitude, resulting in a 565 x 339 array. This grid size provides acceptable computational speed, and is also comparable to the resolution of the depth databases. We note, however, that ETOPO-5 is a gridded data set that has been interpolated from available, irregularly spaced, ship track data. In several parts of the model domain, especially over the southwestern shelves and under the ice shelves, no real depth data are available [see *Padman et al*., 1998]. Additionally, *Smith* [1993] cautioned that the ETOPO-5 bathymetry is generally smoother than the actual topography. He also noted that the interpolation scheme could add unrealistic bathymetric structure in regions without ship tracks.

2.2. *Equations and Boundary Conditions*

Analyses of data from moorings with current meters at more than one depth suggest that tidal kinetic energy in the Weddell Sea is generally dominated by the barotropic (i.e., depth-independent) component. *Middleton and Foster* [1977] found that the barotropic tide accounted for 50% and 72% of the tidal energy in the southern Weddell Sea, for the semidiurnal and diurnal constituents, respectively. Data from Ice Station Weddell, in the western Weddell Sea, showed that there was only a very small velocity difference between currents at 50 m and 200 m below the drifting ice camps [*Levine et al.*, 1997], again consistent with a predominantly barotropic tide. For this first modeling effort, therefore, we have chosen a two-dimensional, depth-integrated barotropic model and therefore ignore variations of currents with depth.

The model uses the mass conservation and depth-integrated shallow water momentum equations:

$$\eta_t + \frac{\partial U}{\partial x} + \frac{\partial V}{\partial y} = 0 \qquad \textbf{(1)}$$

$$U_t = \underbrace{-\frac{U}{H}\frac{\partial U}{\partial x} - \frac{V}{H}\frac{\partial U}{\partial y}}_{\text{Advection}} + \underbrace{2\Omega \sin\theta V}_{\text{Coriolis}} - \underbrace{\beta g H \frac{\partial \eta}{\partial x}}_{\text{Pressure}}$$

$$\underbrace{-\frac{C_D U|\mathbf{U}|}{H^2}}_{\text{Bottom Stress}} + \underbrace{A_H\left(\frac{\partial^2 U}{\partial x^2} + \frac{\partial^2 U}{\partial y^2}\right)}_{\text{Lateral Viscosity}} + \underbrace{F_U}_{\text{Astronomical Forcing}} \qquad \textbf{(2a)}$$

$$V_t = \underbrace{-\frac{U}{H}\frac{\partial V}{\partial x} - \frac{V}{H}\frac{\partial V}{\partial y}}_{\text{Advection}} - \underbrace{2\Omega \sin\theta U}_{\text{Coriolis}} - \underbrace{\beta g H \frac{\partial \eta}{\partial y}}_{\text{Pressure}}$$

$$\underbrace{-\frac{C_D V|\mathbf{U}|}{H^2}}_{\text{Bottom Stress}} + \underbrace{A_H\left(\frac{\partial^2 V}{\partial x^2} + \frac{\partial^2 V}{\partial y^2}\right)}_{\text{Lateral Viscosity}} + \underbrace{F_V}_{\text{Astronomical Forcing}} \qquad \textbf{(2b)}$$

where η is the height above mean sea level, U and V are volume transports in the east-west and north-south directions, respectively, and $\mathbf{U}$ $(=Ui+Vj)$ is the volume transport vector. In the open ocean, $H(x,y)$ represents the water depth, while under the ice shelves it represents the water column thickness. In the Coriolis term, Ω is the angular rotation of the earth ($=7.292\text{x}10^{-5}\ s^{-1}$) and θ is the latitude. The pressure term includes g, the gravitational acceleration ($9.8\ m\ s^{-2}$), and a simplified scalar factor to correct for tidal loading and ocean self-attraction (β = 0.9) [*Schwiderski*, 1980]. Bottom frictional stress is represented by a quadratic drag formulation with a drag coefficient, C_D, of 0.003. We chose this value because it was within the range of observed values, 0.001 to 0.003 [*Gallagher and Munk*, 1971], and is similar to those used in other numerical models, [e.g. *Ramming and Kowalik*, p. 17, 1980; *MacAyeal*, 1984; *Parker*, 1991; *Kowalik and Proshutinsky*, 1994; *Le Provost et al.*, 1994]. Sensitivity tests in which C_D was varied between 0.0025 and 0.0035 indicate only minor variations in tidal heights and currents. Under the ice shelves, C_D was doubled to account for the additional drag at the ice/water interface [*MacAyeal*, 1984]. The ice shelf edge location was obtained from the *Central Intelligence Agency* [1972] coastline data set (**Figure 1a**).

A lateral viscosity coefficient, (A_H) of 1000 m^2s^{-1} is used. This value is at the top of the range of 50-1000 m^2s^{-1} used in the Arctic by *Kowalik and Proshutinsky* [1994], and is an order of magnitude higher

than that used in the Ross Sea (100 m^2s^{-1}) by *MacAyeal* [1984]. It is, however, within the range of estimated values and provides the necessary model stability. The forcing functions for the velocities, F_U and F_V, are determined from the astronomical tide-generating potentials [e.g., *Cartwright and Taylor*, 1971] and corrected for solid earth tides in the standard way.

Four tidal constituents were modeled, two semidiurnal (M_2 and S_2), and two diurnal (O_1 and K_1). Although the relative strengths of tidal constituents vary with location, these four constituents generally account for about 70-80% of the total tidal elevation [*Pond and Pickard*, 1978, p 260]. The available tidal elevation data in our model domain support this estimate.

For land boundaries, both the no-normal flow and no-slip conditions are used. At open boundaries, setting either the elevation or the normal flow leads to a mathematically well-posed problem. We used tide height coefficients obtained from TPXO.3, an updated version of the global inverse solution described in *Egbert, Bennett, and Foreman* (*EBF)* [1994] based on assimilation of approximately three years of TOPEX/Poseidon altimetry data. This model was chosen due to its availability and its known good performance [*Andersen et al.*, 1995].

The model was implemented on a Thinking Machines CM-5. A 12 s time step was used to satisfy the *Courant-Friedrichs-Levy* stability condition [*Haltiner and Williams*, 1980]. The model simulations were run for 105 days. For the parameters we used, the model stabilized after approximately 50 days. After stabilization, the model elevation results were harmonically analyzed for 45 days, producing fields of the amplitude and phase for each tidal constituent. The velocity components were also harmonically analyzed for 45 days to obtain estimates of the major and minor axes, inclination, and phase for the tidal ellipses, following the definitions of *Foreman* [1978].

2.3 *Sources of Error in the Model*

The primary sources of error for the model are uncertainties in boundary conditions and bathymetry, and the use of simplified shallow water equations (including the barotropic assumption). The boundary condition errors are dependent on the quality of the TPXO.3 global solution. For our model domain, the worst performance for TPXO.2 (the global model that preceded TPXO.3) was in Drake Passage where root mean square (rms) differences were 3.6, 1.3, 1.3, and 1.0 cm for the M_2, S_2, O_1, and K_1 constituents, respectively [*Andersen et al.*, 1995]. These estimates should be viewed as upper limits, however. They were generated when only one year of altimetry data was available for the *EBF* model. Presently, the *EBF* model incorporates three years of altimetry data and its performance has improved significantly, particularly in the region of Drake Passage and the Patagonian Shelf.

In the shallow water equations, the physics for both the bottom stress term and the lateral viscosity term have been parameterized and thus are potential sources of error. Exclusion of processes such as baroclinicity, and stress at the interface separating the sea ice from the ocean, are additional error sources. We believe, however, that poor bathymetric information is likely to be most significant single error source for our model. The bathymetry is poorly known in several parts of the model domain, especially over the southwestern shelves [see *Padman et al.*, 1998], and under the ice shelves. *Padman et al.* [1998] demonstrate that changing the model bathymetry based on observations of iceberg grounding [*Viehoff and Li*, 1995] can change predicted currents in some regions of our model by as much as a factor of four.

3. VALIDATION DATA

3.1. *Elevation Measurements*

Two types of elevation measurements, satellite altimetry and tide gauges, were available for comparison with the model. The satellite data consist of coefficients determined by harmonic analysis of sea surface elevation at 356 crossover points from three years of TOPEX/Poseidon data (1993-1996). The southern limit for these data is about 66°S. Tide gauge data consist of elevation time series at a few coastal stations on the Antarctic continent in the Weddell Sea [*Smithson*, 1992; *Genco et al.*, 1994], and several records obtained from the "open" water [*Middleton and Foster*, 1977; *Middleton et al.*, 1982, 1987; *Lutjeharms et al.*, 1985; *Foldvik et al.*, 1990] and under the FRIS [*Thiel et al.*, 1960; *Pratt*, 1960; *Hisdal*, 1965; *Stephenson et al.*, 1979; *Eckstaller and Miller*, 1984; *Smith*, 1991; *Doake*, 1992]. Thirty-one elevation observations were found within the model domain (**Figure 2a**). These observations are summarized in **Table 1**, using the first author of each reference as an identifier. (For the *Genco et al.* [1994] and *Pratt* [1960] observations, measurements were published only for the M_2 constituent.) Twenty-one observations were in open water and ten records were obtained under, or at the edge of, an ice shelf (**Figure 2a**). Five of the ice shelf observations were dis-

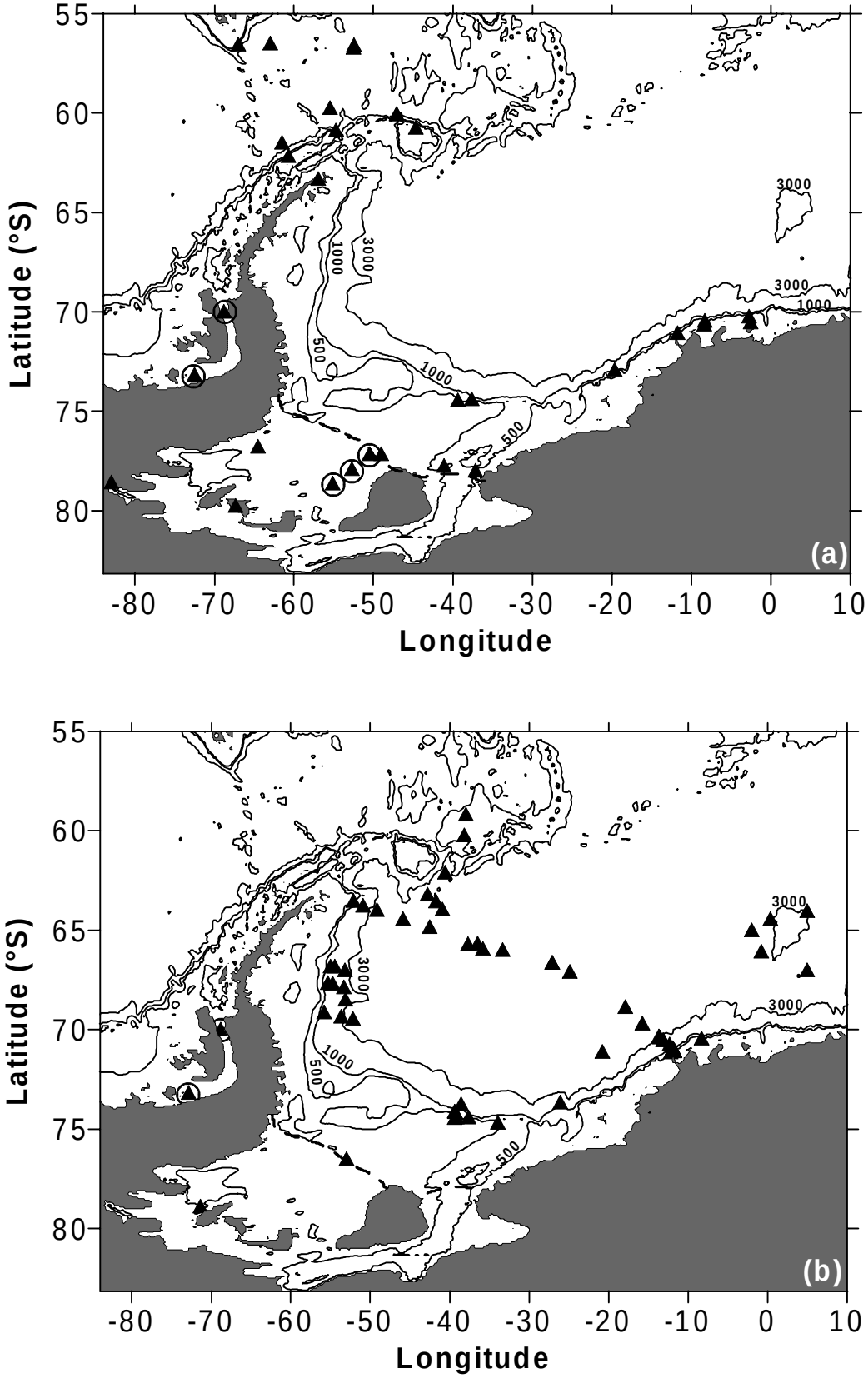

Fig. 2. (a) The location of the tide gauge observations, with the locations shown as triangles. Circled triangles indicate instruments that were ignored. The 500, 1000, and 3000 m isobaths (or water column thickness isolines under the FRIS) are shown. (b) The locations of the current meter observations, with the locations shown as triangles.

TABLE 1. Tide Gauge Observations for the Weddell Sea

First Author	Year	Latitude	Longitude	Depth observation (m)	Depth model (m)	Record Length (days)	rms error (cm)	Category
Smith	1991	79° 44'S	67° 21'W	N/A	194	43	>12	Ice Shelf
Eckstaller	1984	78° 37'S	55° 8'W	N/A	371	5 to 10	N/A	ignored
Stephenson	1979	78° 33'S	82° 58'W	N/A	10	4	N/A	Ice Shelf
Pratt	1960	77° 58'S	37° 10'W	N/A	481	51	N/A	Open Water
Eckstaller	1979	77° 53'S	52° 45'W	N/A	178	5 to 10	N/A	ignored
Thiel	1960	77° 42.6'S	41° 8.0'W	792	591	30	2,4,8,4 †	Ice Shelf
Eckstaller	1984	77° 8'S	50° 30'W	N/A	236	5 to 10	N/A	ignored
Foldvik	1982a	77° 7'S	49° 3'W	260	252	4.2	3,2,2,2 †	Ice Shelf
Doake	1992	76° 45'S	64° 30'W	N/A	375	9	N/A	Ice Shelf
Foldvik	1985b	74° 26'S	39° 24'W	450	466	30	1	Open Water
Middleton	1982	74° 23'S	37° 39'W	470	521	180	4	Open Water
Potter	1985	73° 8'S	72° 32'W	583	100	357	N/A	ignored
Smithson	1992	72° 53'S	19° 37'W	461	1793	316	N/A	Open Water
Smithson	1992	71° 3'S	11° 45'W	430	416	367	N/A	Open Water
Lutjeharms	1985	70° 37'S	8° 32'W	N/A	107	27	N/A	Open Water
Hisdal	1965	70° 30'S	2° 32'W	N/A	27	3	N/A	Open Water
Smithson	1992	70° 26'S	8° 18'W	468	407	324	N/A	Open Water
Lutjeharms	1985	70° 12.5'S	2° 43.5'W	307	173	20	7	Open Water
Potter	1985	69° 58'S	68° 51'W	512	100	16	N/A	ignored
Genco	1994	63° 17'S	56° 55'W	N/A	188	N/A	N/A	Open Water
Smithson	1992	62° 8'S	60° 41'W	500	369	358	3	Open Water
Smithson	1992	61° 28'S	61° 17'W	3946	4264	320	3	Open Water
Smithson	1992	60° 51'S	54° 43'W	1020	1736	378	4	Open Water
Genco	1994	60° 43'S	44° 39'W	N/A	136	N/A	N/A	Open Water
Smithson	1992	60° 3'S	47° 5'W	2010	2272	408	3	Open Water
Smithson	1992	60° 2'S	47° 6'W	2180	2657	208	3	Open Water
Smithson	1992	59° 44'S	55° 30.'W	3690	3565	377	8	Open Water
Smithson	1992	56° 42'S	52° 32'W	3150	4943	349	5	Open Water
Smithson	1992	56° 40'S	52° 29'W	2891	4218	375	5	Open Water
Smithson	1992	56° 32'S	67° 0'W	500	1162	364	2	Open Water
Smithson	1992	56° 29'S	62° 59'W	3925	3965	320	6	Open Water

† For these two records, rms errors are errors on individual constituents, M_2, S_2, O_1, and K_1, respectively.

The first author and location for the tidal gauge observations. The depth of the observation and the depth used by the model for that location are given along with the record length and rms error. N/A indicates that the quantity is unknown. The category used for comparison against the model results is included. The designation 'ignored' indicates an observation was not included in the determination of the standard deviation of the differences between model results and observations. Multiple values for the uncertainty indicated the uncertainties for the M_2, S_2, O_1, and K_1 constituents, respectively.

carded due either to the instrument type or inaccurate bathymetry. These have been circled in **Figure 2a**.

Two types of instrument were used to obtain tidal elevation under the ice shelves. Tiltmeters measure the tilting of the ice shelf, and gravimeters, which convert variations in gravity to tidal displacements as described by *Thiel et al.* [1960]. *Doake* [1992] compared a tiltmeter and a gravimeter located in close proximity and observed that "the gravity amplitudes were about 30% higher than the amplitudes from the tilt records". He postulated that the ice shelf tilt measurements were erroneous due to the use of an inadequate parameterization of the tidal flexure in their calibration. Consequently, three tiltmeter observations [*Eckstaller and Miller*, 1984] have been excluded from the data comparisons with our model. Because the ETOPO-5 bathymetry under the George VI ice shelf is inconsistent with water depths reported by *Potter et al.* [1985], two tide gauge observations from under the George VI ice shelf [*Potter et al.*, 1985; *Pedley et al.*, 1986] were also excluded from the comparisons (**Figure 2a**).

Both the satellite and the tide gauge data are subject to measurement errors, which need to be considered when determining the quality of the tidal model solution. In standard tidal analysis (see, e.g., *Foreman* [1978]), a set of sine and cosine waves with specific tidal frequencies is fit to the time series of height (or velocity). The resultant coefficients then describe both the amplitudes and the phases of the best-fit tidal constituents. A time series of data residuals can also be calculated, representing that part of the signal that cannot be explained by the set of tidal constituents that were generated by the multivariate fit. Data residuals include instrument errors, as well as true oceanic signals at frequencies that have not been included in the fitting scheme. The latter signals include tidal energy at excluded frequencies, doppler-shifted tidal energy (particularly due to baroclinic currents), and non-tidal energy.

For the satellite data, the estimated error in the amplitude of each tidal constituent was about 3-4 cm. Errors for the tide gauge observations depend on the instrument used to make the measurement. When known, the estimated rms residual error for each measurement is given in **Table 1**. The amplitude error for each tidal constituent in a multivariate fit is provided by the fitting procedure, and is typically much less than the rms residual error. When more than one number is shown in **Table 1**, the numbers represent the reported errors for the M_2, S_2, O_1, and K_1 constituents, respectively. If the rms residual error was not reported, 4 cm was used for the open water measurements and 10 cm for the ice shelf ones. Errors are also larger when the record being analyzed is too short to allow all the energetic tidal constituents to be resolved. At least 15 days of hourly data is required to resolve M_2 from S_2 , and O_1 from K_1, and errors in specific constituents will become much larger as record lengths become shorter than this. Many of the ice shelf observations suffer from short record lengths.

3.2 *Velocity Measurements*

Sixty-four current meter records were found within the model domain (**Figure 2b**). Observations were not used if they were in the bottom boundary layer, defined as within 50 m of the seabed: currents in the boundary layer may not represent the mean water column velocity, which is being simulated by our barotropic model. **Table 2** lists these observations using the first author of the reference as an identifier.

Two of these measurements were made under, or at the edge of, the Ronne Ice Shelf. Ninety-five days of current meter measurements were obtained by deploying a current meter through the ice shelf (K. Nicholls, personal communication, 1996), and *Nygaard* [1995] collected over a year of current meter measurements at a site at the ice shelf edge. Two current meter observations made under the George VI ice shelf [*Potter et al.*, 1985; *Pedley et al.*, 1986] have been excluded in the comparisons because we do not have any reliable bathymetric data in the region surrounding these measurement sites.

Of the sixty open-water locations, thirty observations were provided by *Fahrbach et al.* [1992, 1994], who moored current meters at various locations between the tip of the Antarctic Peninsula and Kapp Norvegia. Most of these moorings provided more than one year of continuous data. At some sites, currents were measured at more than one depth. In these cases we excluded data from within 200 m of the ocean surface. The remaining mid-water column measurements at one site usually agreed with each other within the measurement uncertainty, consistent with our barotropic assumption. For those cases where the observations disagreed, the measurement with the longer time series was used. For two sites, we averaged the mid-water column current meters. One of the *Fahrbach et al.* sites was excluded from the model evaluation because of a large discrepancy between the reported water depth at the measurement location, 415 m, and the model bathymetry, ~1800 m. The velocity is known to be strongly dependent upon bathymetry, therefore comparing modeled and measured currents at this location seemed inappropriate.

First Author	Year	Latitude	Longitude	Depth for observation (m)	Depth for model (m)	Depth of instrument (m)	Record Length (Days)	Category
Nicholls	-	78° 52.0'S	71° 20.3'W	485	525	N/A	95	Ice Shelf
Nygaard	1995	76° 29'S	53° 0'W	431	414	411	435	Ice Shelf
Middleton †	1982	74° 40'S	33° 56'W	475	437	375	410	C. Shelf
Middleton †	1982	74° 26'S	39° 24'W	475	466	375	630	C. Shelf
Middleton †	1982	74° 24'S	39° 6'W	465	448	400	510	C. Shelf
Foldvik	1990	74° 23'S	37° 39'W	475	521	450	31	C. Shelf
Foldvik	1990	74° 8'S	39° 19'W	650	655	627	460	C. Slope
Middleton †	1982	74° 6'S	39° 22'W	720	763	620	600	C. Slope
Middleton †	1982	73° 43'S	38° 36'W	1915	1852	1815	420	C. Slope
Fahrbach	1994	73° 37.6'S	26° 7'W	3360	1658	3197	250	Deep
Fahrbach	1992	72° 52.8'S	19° 37.5'W	415	1793	280	310	ignored
Potter	1985	73° 9'S	72° 49'W	720	100	249	25	ignored
Fahrbach	1992	71° 7.7'S	12° 11.9'W	682	352	255	330	C. Slope
Fahrbach	1994	71° 5.8'S	20° 47.1'W	4440	4289	4277	370	Deep
Fahrbach	1992	71° 3.3'S	11° 44.1'W	380	416	260	300	C. Shelf
Fahrbach	1994	71° 3.0'S	11° 46.0'W	467	416	462	300	C. Shelf
Fahrbach	1994	71° 2.7'S	11° 45.4'W	425	416	325	30	C. Shelf
Fahrbach	1994	71° 2.4'S	11° 44.6'W	676	416	293	360	C. Slope
Fahrbach	1994	70° 59.2'S	11° 49.4'W	2364	481	706	430	C. Slope
Fahrbach	1994	70° 56.4'S	11° 57.7'W	1522	1029	320	420	C. Slope
Fahrbach	1994	70° 54.7'S	11° 57.8'W	1555	1029	760	380	C. Slope
Fahrbach	1994	70° 42.6'S	12° 21.5'W	2123	1760	978	310	C. Slope
Fahrbach	1994	70° 29.7'S	13° 8.9'W	2450	2726	340	400	C. Slope
Fahrbach	1994	70° 29.5'S	13° 7.0'W	2364	2726	856	430	C. Slope
Fahrbach	1992	70° 26.0'S	8° 18.0'W	408	407	330	310	C. Shelf
Fahrbach	1994	70° 22.8'S	13° 32.5'W	2950	3988	940	400	C. Slope
Fahrbach	1994	70° 19.1'S	13° 39.6'W	4330	4392	1130	320	Deep
Potter	1985	69° 58'S	68° 51'W	512	100	N/A	N/A	ignored
Fahrbach	1994	69° 39.6'S	15° 42.9'W	4728	4777	988	430	Deep
Levine	1997	69° 24.9'S	52° 10.3'W	N/A	3217	200	15	Deep
Levine	1997	69° 19.0'S	53° 37.8'W	2700	2890	200	15	C. Slope
Levine	1997	69° 6.8'S	55° 46.1'W	N/A	1535	50	15	C. Slope
Fahrbach	1994	68° 49.7'S	17° 54.5'W	4740	4759	4240	700	Deep
Levine	1997	68° 27.7'S	53° 8.9'W	2900	2584	200	19	C. Slope
Levine	1997	67° 50.2'S	53° 18.4'W	2900	2591	200	15	C. Slope
Levine	1997	67° 40.1'S	54° 43.0'W	N/A	2180	200	15	C. Slope
Levine	1997	67° 37.7'S	55° 18.8'W	N/A	1693	50	15	C. Slope
Fahrbach	1994	67° 3.6'S	24° 52.1'W	4840	4747	4340	400	Deep
Levine	1997	66° 59.4'S	53° 11.4'W	2900	2816	200	15	C. Slope
Bersch	1992	66° 59.2'S	4° 59.4'E	4158	4054	959	180	Deep
Levine	1997	66° 48.7'S	54° 26.9'W	N/A	2238	200	15	C. Slope
Levine	1997	66° 48.5'S	55° 1.0'W	N/A	1721	50	15	C. Slope
Fahrbach	1994	66° 37.4'S	27° 7.1'W	4830	4788	293	430	Deep
Middleton	1977	66° 26.3'S	41°2.6'W	3540		4510	349	Deep
Fahrbach	1994	66° 16.6'S	30° 17.8'W	4750	4788	2840	370	Deep
Bersch	1992	66° 3.2'S	0° 47.1'W	4100	4594	1180	110	Deep
Fahrbach	1994	65° 58.2'S	33° 20.3'W	4800	4896	4300	390	Deep
Barber	1995	65° 55.2'S	35° 49.4'W	4770	4696	4270	270	Deep
Fahrbach	1994	65° 39.9'S	37° 42.5'W	4730	4650	4455	400	Deep
Fahrbach	1994	65° 38.1'S	36° 30.2'W	4710	4701	2534	410/700	Deep
Bersch	1992	64° 58.6'S	2° 0.2'W	4331	5012	901	180	Deep
Fahrbach	1994	64° 48.9'S	42° 29.3'W	4650	4635	1000	400	Deep
Fahrbach	1994	64° 25.1'S	45° 51.0'W	4390	4434	220	430	Deep
Bersch	1992	64° 24.5'S	0° 22.2'E	5019	3624	1120	180	Deep
Bersch	1992	64° 1.2'S	1° 20.8'E	3721	2844	1043	180	Deep

Fahrbach	1994	63° 57.0'S	49° 9.2'W	3480	3279	2970	420	Deep

First Author	Year	Latitude	Longitude	Depth for observation (m)	Depth for model (m)	Depth of instrument (m)	Record Length (Days)	Category
Barber	1995	63° 56.6'S	40° 54.0'W	4575	4554	4075	350	Deep
Fahrbach	1994	63° 45.1'S	50° 54.3'W	2460	2286	2410	430	C. Slope
Barber	1995	63° 31.0'S	41° 45.9'W	4580	4299	4030	350	Deep
Fahrbach	1994	63° 29.6'S	52° 6.3'W	940	733	260	240	C. Slope
Barber	1995	63° 10.7'S	42° 46.0'W	3855	3660	3355	350	Deep
Barber	1995	62° 4.5'S	40° 35.7'W	3375	3352	3365	340	Deep
Barber	1995	60° 11.3'S	38° 8.6'W	2969	3133	2959	290	C. Slope
Barber	1995	59° 8.8'S	37° 57.6'W	2870	2930	2070	160	C. Slope

† *Foldvik et al.* [1990] is a more useful reference for these observations.

The first author and location for the velocity observations. The depth of the observation and the depth used by the model for that location are given along with the record length. C. = continental; other terms are as defined in Table 1.

Ten observations were provided by *Levine et al.* [1997], who analyzed current meters located at 50 m and 200 m below the various camps of Ice Station Weddell. Since the camps were moving, the current meter data were broken into 15-day segments for analysis. The average location for the camp during each time segment was used for the observation location. Eight observations were collected as part of a Weddell Sea tidal study [*Foldvik and Kvinge*, 1974; *Middleton and Foster*, 1977; *Foldvik et al.*, 1982a,b, 1985a,b; *Middleton et al.*, 1982, 1987; *Foldvik et al.*, 1990]. All but one of these observations were made in the southwestern Weddell Sea near the shelf/slope break, and record lengths were typically from one to two years. A mid-basin observation described in these studies was excluded because the current meter was within 30 m of the bottom [*Middleton and Foster*, 1977]. *Barber and Crane* [1995] made seven observations near the tip of the Antarctic Peninsula. Finally, five observations with lengths of about a half-year were collected by *Bersch et al.* [1992] near Maud Rise. *Foreman*'s [1978] analysis software was used to determine the tidal constituents for these observations.

As with the elevation data, estimates of velocity errors are needed before measurements can be used to evaluate model performance. Typical rms residual errors for the *Levine et al.* [1997] and *Bersch et al.* [1992] records were about 2-3 cm s^{-1}, with the exception of the two northernmost Ice Station Weddell camp locations, which had values of about 6 cm s^{-1}. We attribute these higher residual errors to greater motion of the camp during this time period. For locations for which error estimates were not available, we used an rms residual error of 2 cm s^{-1}, which is consistent with the measurement error for Aanderaa current meters [*Aanderaa Instruments*, 1979]. Record length is also a significant factor in the accuracy of the tidal constituents: errors increase with shorter record length, and are particularly severe for records of less than 30 days. As described in section 3.1, the error on individual constituent velocities will be less than the rms residual error. For comparison purposes, the uncertainty in each constituent was therefore taken to be 1 cm s^{-1}, which represents a relatively small percentage error for regions of strong tidal flows in our model.

4. MODEL RESULTS

4.1 *Tidal Elevations*

The largest tidal elevations are due to the semidiurnal constituents. The M_2 constituent has a tidal amplitude greater than 1.5 m at the southwestern end of the Ronne Ice Shelf (**Plate 1a**), and greater than 1.0 m under the Larsen Ice Shelf. For M_2, there are two amphidromic points, one in the northeastern Weddell Sea and one near the edge of the Ronne Ice Shelf. Phase generally propagates from east to west along the Antarctic continent, and clockwise under the FRIS. The S_2 constituent (**Plate 1b**) is structurally similar to M_2, although it's amplitude is smaller and there is an additional amphidromic point near the tip of South America.

The tidal amplitude for the diurnal constituent, K_1, generally increases towards the Antarctic continent, except for an area along the outer southern shelf including the General Belgrano Bank (**Plate 1c**). The structure of the O_1 constituent (**Plate 1d**) is very similar to K_1. No amphidromic points occur within our model domain for the diurnal constituents, and the phase propagates roughly from east to west, except for a region of complex structure along the southern slope, which can be ascribed to the presence of diurnal shelf waves along the southern shelf and slope. These shelf modes will be considered in more detail in a future study.

4.2. *Tidal Velocities*

The lengths of the major axes for the modeled current ellipses (U_{maj}) for the M_2 and O_1 components are shown in **Plate 2**. The value of $U_{maj}(M_2)$ exceeds 5 cm s^{-1} over most of the shelf and upper slope. Values greater than 30 cm s^{-1} are found under the leading edge of the Ronne Ice Shelf west of Berkner Island, on the Patagonian Shelf, under the Brunt and Riiser-Larsen Ice Shelf (near 20°W on the Antarctic coast), and in Bransfield Strait. Other regions of strong M_2 currents are: the General Belgrano Bank; a region from 15°W to 25°W along the Antarctic coast; and much of the western Weddell Sea shelf adjacent to, and under, the Larsen Ice Shelf.

For the diurnal constituents, $U_{maj}(O_1)$ is largest over the General Belgrano Bank, exceeding 75 cm s^{-1} in this region. Other regions of strong diurnal currents include: the entire outer shelf in the southern Weddell Sea; the front of the Ronne Ice Shelf; and near the northern tip of the Antarctic Peninsula, including Bransfield Strait and the South Orkney Plateau. Diurnal tides are expected to exist in these regions as topographically-trapped shelf modes, and thus tend to be strongest over the upper continental slope where the bottom slope is steep and the water depth is relatively shallow [*Loder*, 1980; *Middleton et al.*, 1987; *Padman et al.*, 1992]. Because of the sensitivity of diurnal currents to topography, rela-

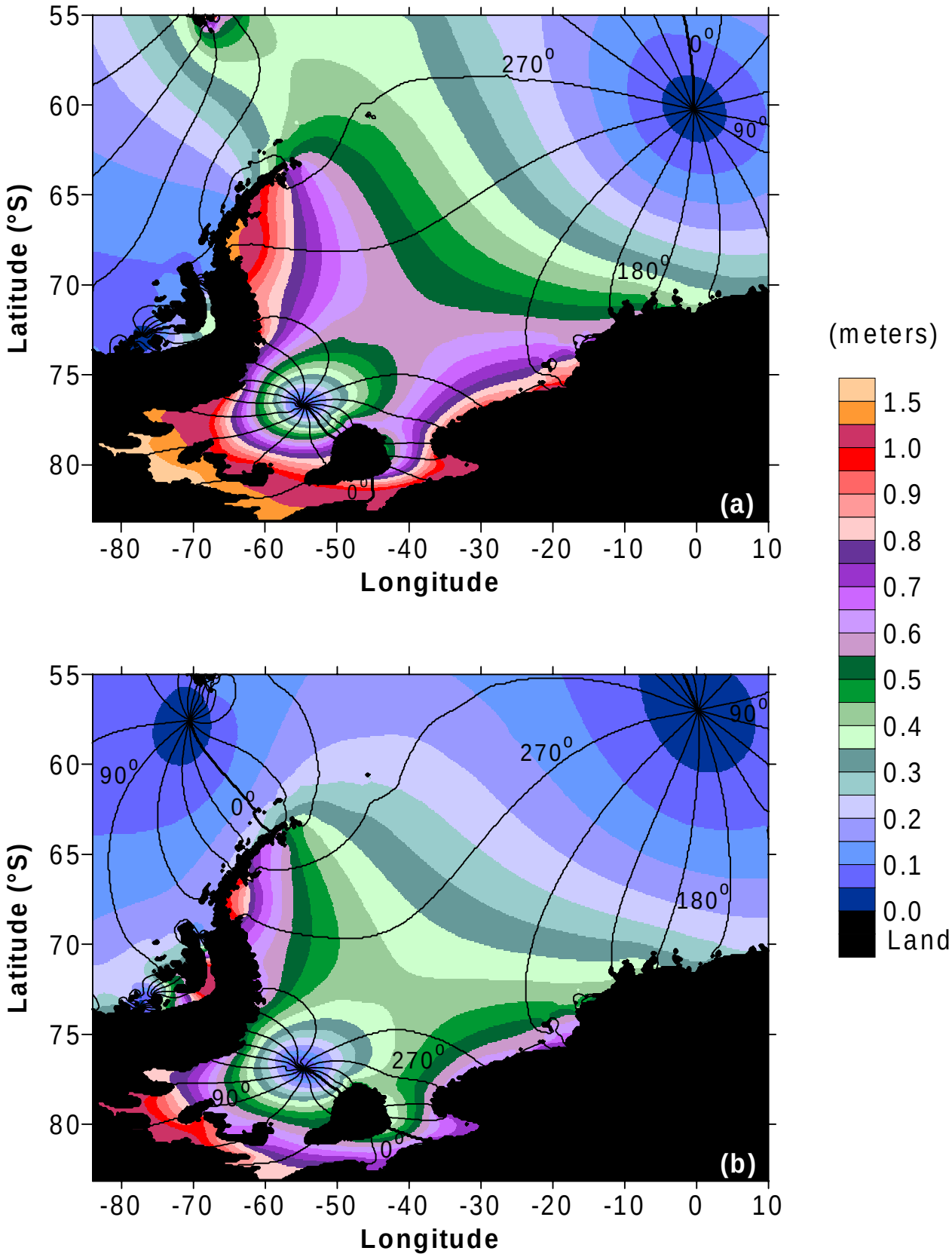

Plate 1. The elevation amplitude and phase for the (a) M_2, (b) S_2, (c) K_1, and (d) O_1 constituents, with the amplitude given by the color scale and the phase by the contour lines. The contour interval is 22.5^o in phase.

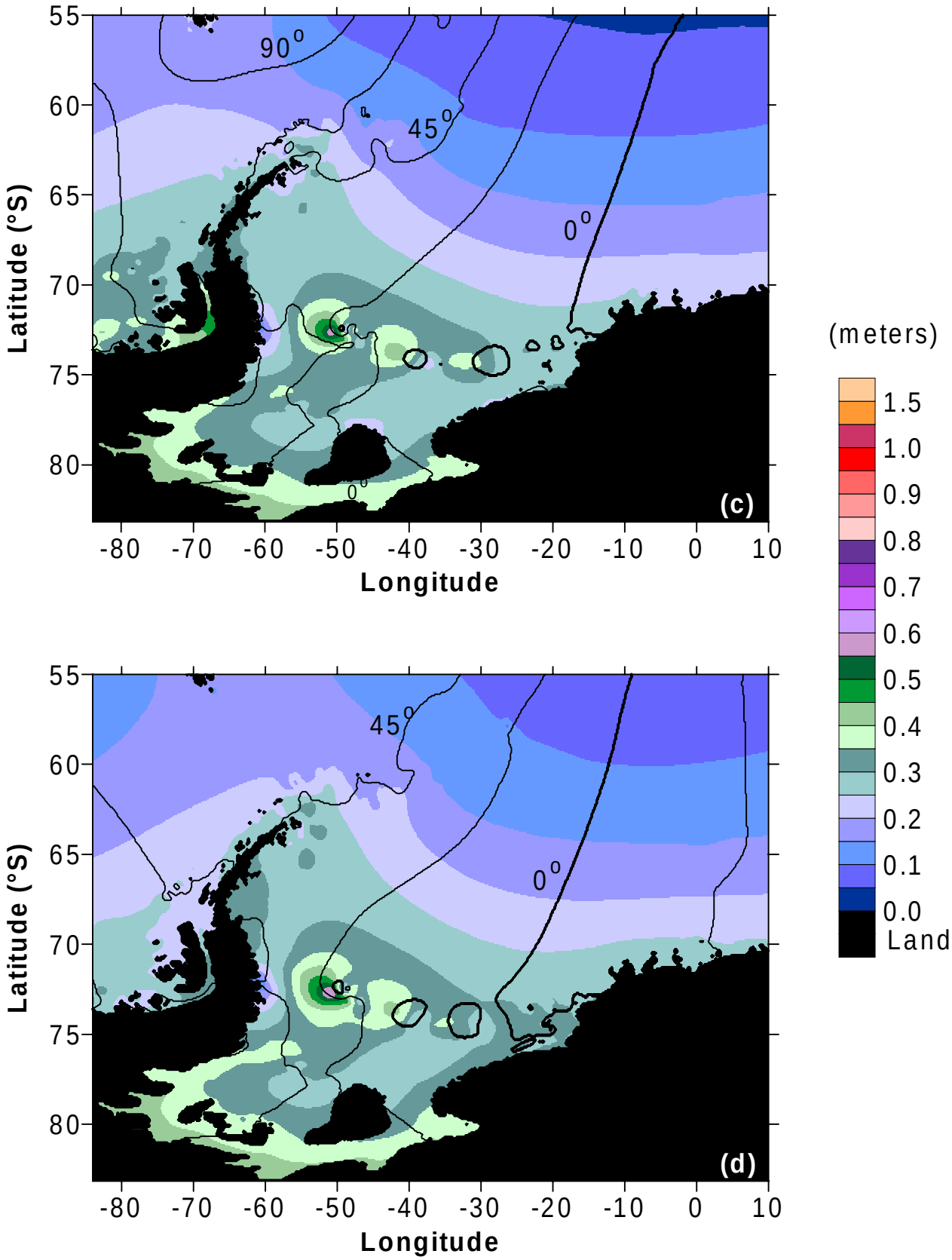

Plate 1. The elevation amplitude and phase for the (a) M_2, (b) S_2, (c) K_1, and (d) O_1 constituents, with the amplitude given by the color scale and the phase by the contour lines. The contour interval is 22.5^o in phase.

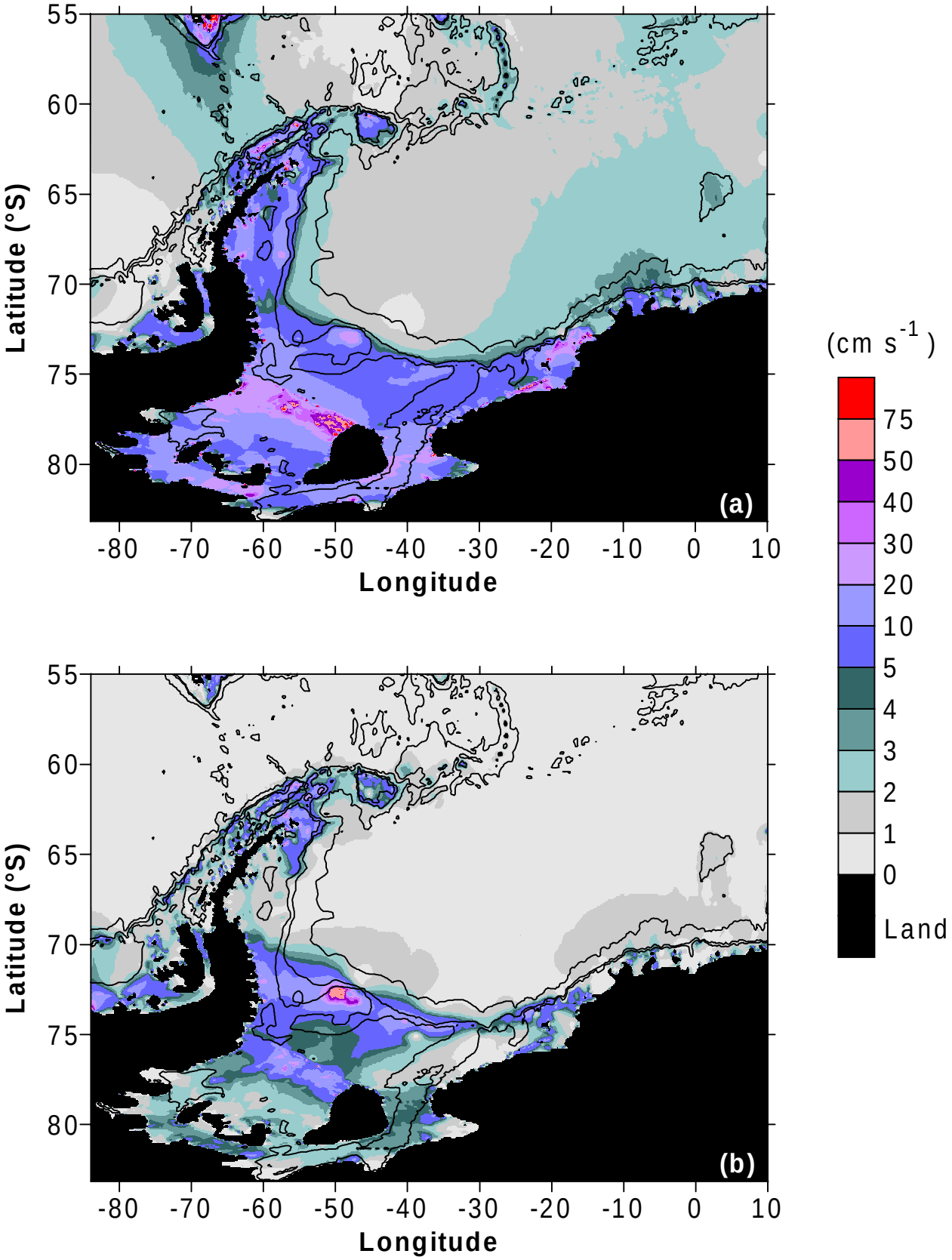

Plate 2. Length of major axis of the modeled tidal ellipse for (a) the M_2 and (b) O_1 constituents. Isobaths (or water column thickness isolines under the FRIS) for 500, 1000, and 3000 m are shown. Note that the color ranges are not evenly spaced.

tively small errors in bathymetry can radically alter the modeled currents. We have made several model runs with varying bathymetry to investigate this sensitivity, and some comparisons will be presented by *Padman et al.* [1998]. One sensitivity run involved modifications of the southern shelf/slope between 50°W and 60°W, in a region with very little available bathymetric data. It is possible, with model bathymetry that is not inconsistent with available depth data, to reduce $U_{maj}(O_1)$ over the General Belgrano Bank to less than 20 cm s^{-1}, i.e., less than 25% of the value shown in **Plate 2b**. At present we favor the lower value of $U_{maj}(O_1)$ for this region, based on observed tidal-frequency ice motion [*Padman et al.*, 1998]. However, the results shown here are appropriate for the bathymetry given by GEBCO chart 5.18 with the revisions we have made based on *LaBrecque and Ghidella* [1993].

The relationship between tidal currents and bathymetry can be seen in transects of $U_{maj}(M_2)$ and $U_{maj}(O_1)$ (**Figure 3**) along the lines A-A', B-B', and C-C' (**Figure 1b**). As we noted above, the strongest M_2 currents tend to occur in shallow water, e.g., at the front of the Ronne Ice Shelf (~77°S in **Figure 3b**) and over the broad southern shelf (south of ~74°S in **Figure 3c**). Diurnal currents are usually strong at the upper continental slope and at other rapid changes in bathymetry. One exception is over the narrow shelf near Kapp Norvegia (**Figure 3a**): this is typical of most of the Antarctic coastline east of about 20°W in our model (**Plate 2b**).

A useful measure of a typical tidal current magnitude is given by

$$u_{typ}^2 = \sum_{i=1}^{4} \left(u_i^2 + v_i^2\right), \qquad \textbf{(3)}$$

where u_i and v_i are the amplitudes of the east and north components of velocity for tidal constituent '*i*'. Values of u_{typ} are usually small over the deep basin but increase to over 5 cm s^{-1} near the shelf break (**Plate 3**). Currents greater than 10 cm s^{-1} are common over the continental shelves and are significantly larger than the mean boundary currents of 4-6 cm s^{-1} [*Fahrbach et al*., 1994] associated with the Weddell Gyre. The largest tidal currents occur in regions where the bathymetry changes rapidly. Maximum values of u_{typ} are greater than 1 m s^{-1} and occur near General Belgrano Bank, where diurnal constituents dominate the total tidal signal (**Plate 2b** and **Figure 3b**). Velocities greater than 75 cm s^{-1} also occur under the Ronne Ice Shelf near the ice front, where semidiurnal constituents dominate (**Plate 2a** and **Figure 3b**).

4.3. *Comparisons Between Model Results and Measurements*

4.3.1. Elevations. For comparison purposes, the model domain was broken into two categories: open water; and under the ice shelf or at its edge (**Table 1**). All of the satellite altimetry data lie in the open water. Twenty-one non-satellite tidal elevation measurements are in the open water category and five in the ice shelf category. For each measurement location and for each tidal constituent, we first calculate the difference (δ_i) between the model-predicted elevation amplitude ($a_{m,i}$) and the amplitude based on data ($a_{d,i}$), where subscript '*i*' identifies a specific tidal constituent. Then, for each ocean category with *M* comparison sites, we determine the standard deviation of δ_i. A similar calculation is made for phase. These values are given in **Table 3**. The equivalent rms percentage errors, for amplitudes, were determined from $\{M^{-1}\Sigma[(100\delta_i/a_{d,i})^2]\}^{½}$, where the rms error is used for $a_{d,i}$ if $a_{d,i}$ is less than the rms error.

Model results agree quite well with the satellite data. The standard deviation of the differences between the model results and measurements, for all four constituents, were 3 cm or less in amplitude and 9 to 32° in phase. Good agreement was found for tide gauge data in the open water. The standard deviation of the amplitude errors was 5 cm or less, and 5-8° for phase. The percentage error for these standard deviations ranged from 8 to 19%, which is lower than the percentages for the satellite data, 16 to 47%. Since the percentages are based on the magnitude of the elevation, and the elevations are typically larger in the shallower water where the tidal gauges are usually located, equivalent absolute differences for the standard deviation result in smaller percentages. Under the ice shelves, the agreement between model results and measurements was poorer, with standard deviation errors of 8-14 cm for amplitude and 12-70° for phase. The largest phase errors under the ice shelves were associated with the diurnal constituents. Due to the higher mean amplitudes, the percentages of error for these standard deviations were still reasonably low, less than 25% except for S_2.

Comparisons of model elevation coefficients and measurements are shown in **Figures 4a-d** for the M_2, S_2, O_1, and K_1 constituents, respectively. As we noted above, there are a variety of reasons for mismatches between the model output and data. The two error sources that are believed to be most important are model response to errors in bathymetry and constituent errors in the data due to short analysis record

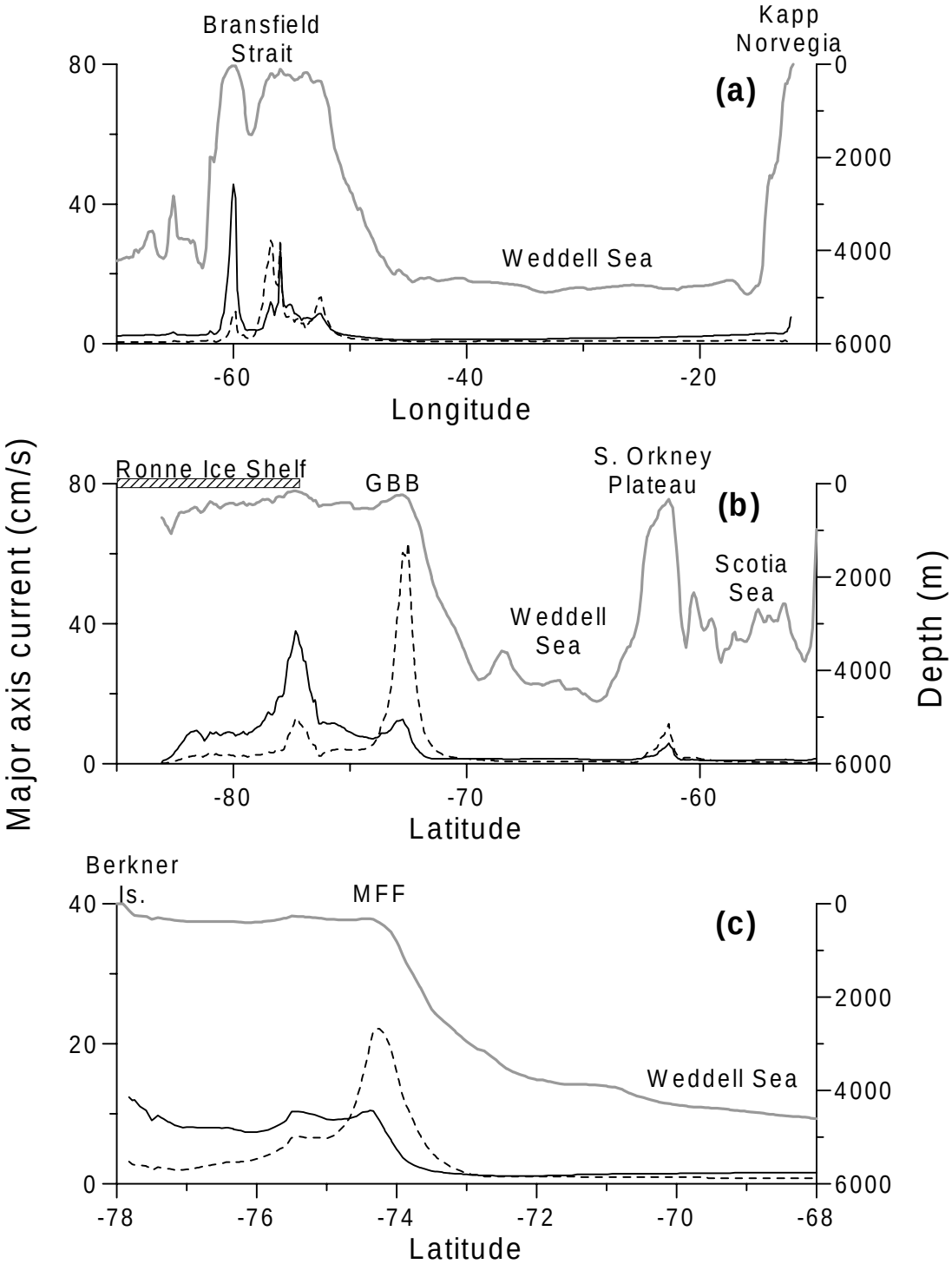

Fig. 3. Transects of bathymetry (gray line) and M_2 and O_1 major axis lengths (solid line, $U_{maj}(M_2)$; dashed line, $U_{maj}(O_1)$) for the three transects on Figure 1b: (a) transect A-A'; (b) transect B-B'; (c) transect C-C'. Features shown include the General Belgrano Bank ("GBB" in (b)), and the *Middleton et al.* [1987] moorings ("MFF" in (c)).

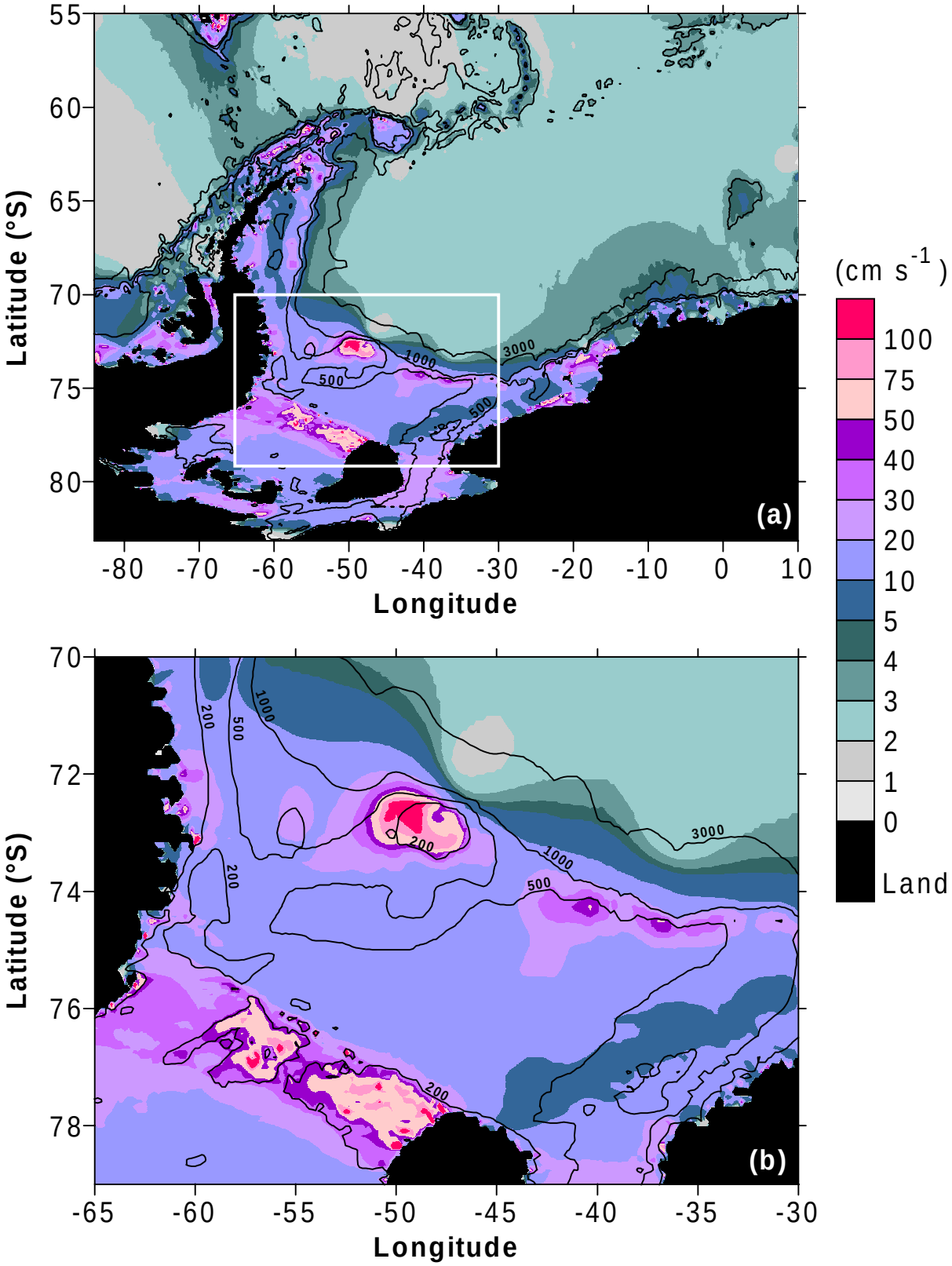

Plate 3. (a) The combined typical current speed (U_{typ}: (eq. 3)) for the four principal tidal constituents for the entire model domain. The 500, 1000, and 3000 m isobaths (or water column thickness isolines under the FRIS) are shown. (b) As for (a), but for only the central southern shelf region. The 200 m water column thickness line has been added. Note that the color ranges are not evenly spaced.

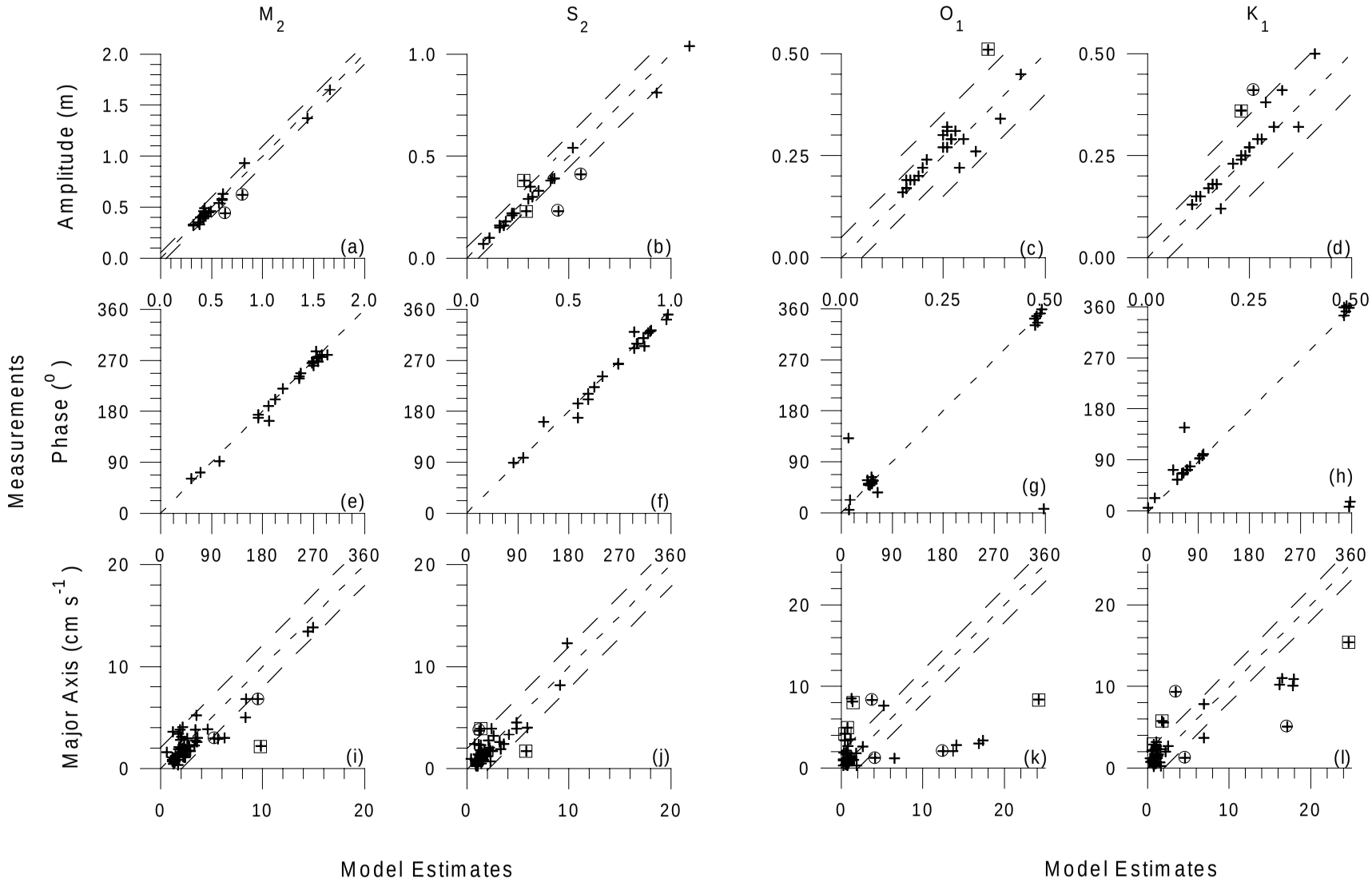

Fig. 4. The correlation between the model results and the observed harmonic constituents for (a-d) the tidal elevation, (e-h) phase for the elevation, and (i-l) major axis for the M_2, the S_2, the O_1, and the K_1 constituents, respectively. The short-dashed line represents perfect agreement between the model results and the measurements: the area above the line indicates under-prediction by the model. The long-dashed lines represent estimates of general measurement uncertainties. Observations with short record lengths have been indicated with squares and those believed to have inaccurate topography with circles.

TABLE 3. The standard deviations of the differences between the model elevation results and the observations for the two categories, open water and at the edge of or under the ice shelf.

Model	Category	Data Source	N[a]	M_2		S_2		O_1		K_1	
				A[b] (cm)	Phase (°)	A[b] (cm)	Phase (°)	A[b] (cm)	Phase (°)	A[b] (cm)	Phase (°)
Robertson et al.	Open Water	Satellite Data	356	2 (16 %)	16	3 (47 %)	32	1 (16 %)	9	3 (25 %)	20
Robertson et al.	Open Water	Tide Gauges	18 (21 for M_2)	5 (8 %)	7	3 (13 %)	8	2 (8 %)	5	5 (19 %)	6
Robertson et al.	Under the Ice Shelf	Tide Gauges	5	12 (24 %)	12	14 (51 %)	20	8 (16 %)	62	9 (22 %)	70
TPXO.3: Egbert et al.	Open Water	Tide Gauges	17 (19 for M_2)	5 (11 %)	11	4 (12 %)	12	2 (8 %)	7	4 (20 %)	5
FES95.2: Le Provost et al.	Open Water	Tide Gauges	17 (19 for M_2)	5 (12 %)	26	6 (29 %)	38	5 (19 %)	18	4 (20 %)	20
AG95: Andersen-Grenoble	Open Water	Tide Gauges	15 (16 for M_2)	3 (28 %)	8	1 (19 %)	5	3 (33 %)	26	2 (14 %)	31

a. Number of Observations
b. Amplitude
For the open water comparison, the differences were determined both for the satellite data and the tidal gauge data. The corresponding percentages are shown for the amplitudes. The number of points used in each comparison is shown, with the parenthesis indicating the number for the M_2 constituent if it had a different number of observations. The standard deviations of the differences in open water are also shown for the *Egbert et al*. (TPXO.3), *Le Provost et al*. (FES95.2), and the *Andersen-Grenoble* (AG95) models .

lengths as identified on **Figure 4**. Points where the model amplitude estimates differ by more than 25% from data are examined in Appendix A. The phases agree well for most measurement locations and constituents (**Figures 4e-h**).

4.3.2 Velocities. The model velocities were compared with the sixty velocity measurements described in Section 3.2. Except for the major axis, the tidal ellipse descriptors are very unstable when velocities are low. We therefore compared only the modeled and measured major axes of the tidal ellipses, and ignored the other three descriptors, the minor axis, inclination, and phase. Model velocities at each location were adjusted by the ratio of the model water depth to the reported depth for the measurement site; i.e., we actually compared the depth-integrated barotropic transports. The domain was broken into three water depth categories, the continental shelf, the continental slope, and deep water, and a fourth category for the area under the ice shelf or at its edge (**Table 2**). Eight data points are located on the continental shelf, which was defined as having a depth of less than 500 m and not being under an ice shelf. Twenty-five data points are located on the continental slope, with depths ranging from 500 to 3000 m. Twenty-five data points are located in deep water, with depths greater than 3000 m. Two points are in the ice shelf category.

The standard deviation of the differences between the major axis from the model and that of the measurement (**Table 4**) was calculated in the same manner as for the elevations (section 4.3.1, above). In deep water, velocities were small and the standard deviations of the differences were less than or equal to 1.5 cm s^{-1}. For the continental slope, the standard deviations of the differences were larger 1.2-4.8 cm s^{-1} (57-131%). On the continental shelf, standard deviations were as large as 1.9 cm s^{-1} (55%) for semidiurnal constituents, and 6.8 cm s^{-1} (266%) for the diurnal constituents. The large errors for the diurnal constituents are probably associated with the presence of topographically trapped, diurnal shelf waves [*Middleton et al.*, 1987]. These waves are sensitive to both the along-slope and cross-slope topography. Our model predicts amplification for the O_1 constituent that was not observed by *Middleton et al.* [1987]. For the ice shelf regions, the standard deviations of the model misfits reached 3.5 cm s^{-1}.

The correlations between the model and measured velocities are shown for the four constituents in **Figures 4i-l**. The convention is the same as used for the elevation comparisons. The primary error sources are again inaccurate model bathymetry and measurement errors, particularly due to short record lengths. Baroclinicity is an additional error source for the velocities. The largest discrepancies between the model velocities and the measurements are discussed in Appendix B.

4.4 *Comparison of Model Results with Three Global Models*

We evaluate the effect of increased resolution, improved bathymetric data, and the explicit inclusion in our model of the ocean cavity under the FRIS, by comparing the results of our model with three global tidal models: TPXO.3 [*EBF*], FES95.2 [*Le Provost et al*., 1994], and AG95 [*Andersen*, 1995]. These comparisons were only made for the open water regions. The standard deviations of the elevation differences were calculated for this model, following the procedure described in section 4.3.1. Since the model domains cover slightly different areas, some of the tidal gauge locations are not included in all domains. The number of locations used for each of the calculations is given in **Table 3**. Our model reproduced measured tidal elevations slightly better than TPXO.3 and FES95.2 in the open water for the semidiurnal constituents. The AG95 model has lower standard deviations for the differences, but higher percentage errors. As its does not include some areas where several of the shallower tide gauges were located, the AG95 standard deviations are biased toward the smaller elevations of deeper water, resulting in smaller values with higher corresponding percentages. Thus, the smaller standard deviations of the differences for AG95, which does not include our entire model domain, do not necessarily indicate improved performance.

Velocities were not available for the FES95.2 and AG95 models. Therefore, only the TPXO.3 model was used for a velocity comparison. Although the elevations were similar, the TPXO.3 model does not generate the high velocities seen in our model. This was particularly evident in the shallower water in the southern portion of the domain and at the continental shelf/slope break. The velocities at the southern slope/shelf break, where short-wavelength, topographically trapped shelf waves occur, were underpredicted by ~10 cm s^{-1} by *EBF* for K_1, compared to our overprediction of ~5 cm s^{-1}. The higher currents in our model can be attributed to improved bathymetry and higher grid resolution.

TABLE 4. Standard deviations of the differences between the model velocity major axes and the observations for the four categories shown, with the corresponding percentages.

Category	M_2	S_2	O_1	K_1
Continental Shelf	1.9 (55 %)	0.8 (21 %)	6.8 (266 %)	5.2 (84 %)
Continental Slope	2.0 (83 %)	1.2 (57 %)	4.8 (131 %)	2.7 (57 %)
Deep	0.7 (43 %)	0.5 (35 %)	1.5 (95 %)	0.9 (26 %)
Ice Shelf	1.4 (44 %)	2.8 (97 %)	2.7 (32 %)	3.5 (45 %)

5. TIDAL ENERGY BALANCE

5.1. Tidal Energy Flux

For any region of the model domain, the tidal energy balance can be written as:

$$\oint_L \langle E n dl \rangle + \iint_{Area} \langle \mathbf{F}(x,y) \cdot \mathbf{u} \rangle dx\,dy - \iint_{Area} \langle D(x,y) \rangle dx\,dy = 0 \qquad \textbf{(4)}$$

where E_n is the energy flux normal to the closed boundary (L), $\mathbf{F}(x,y)$ represents local astronomical forcing corrected for solid earth tides, $D(x,y)$ represents the sum of local dissipation terms, and angle brackets represent time averaging. The dissipation term includes bottom friction and lateral friction, which are both parameterized in our model. Recall that the friction between the glacial ice shelves and the ocean has been represented by doubling C_D in these regions. Other dissipative terms that we have not modeled include stress at the interface between sea ice and the ocean, "topographic drag" (i.e., energy input into baroclinic motion such as internal tides), and ice shelf flexure.

The first term in (4) is the energy flux divergence, which balances any energy production ($\langle \mathbf{F} \cdot \mathbf{u} \rangle$) and dissipation ($D$) within the area enclosed by L. For each constituent, the components of energy flux at any point in the model domain, averaged over a complete tidal period, are

$$E_u = 0.5 \rho\, g\, \beta\, H\, A_u\, A_\eta \cos(\theta_u - \theta_\eta), \qquad (5a)$$

and

$$E_v = 0.5 \rho\, g\, \beta\, H\, A_v\, A_\eta \cos(\theta_v - \theta_\eta). \qquad (5b)$$

In (5), H is the water depth, A_u, A_v, and A_η are the constituent amplitudes for the east/west velocity, the north/south velocity, and the elevation respectively, and θ_u, θ_v, and θ_η are the associated phases. As in (2), the factor β=0.9 is applied as a simple correction for ocean loading and self-attraction [*Egbert*, 1997]. The factor of 0.5 arises from time averaging over a complete tidal cycle.

On average, the energy flux is clockwise around the Weddell Sea for all constituents. For M_2 (**Plate 4a**), the flux is westward along the Antarctic coast, turning southward under the FRIS, primarily through the Filchner Depression. This energy under the FRIS propagates clockwise and emerges at the western end of the Ronne Ice Shelf, then flows northwards along the eastern side of the Antarctic Peninsula, across Drake Passage and up the east coast of South America. Significant energy also flows around the Patagonian shelf from the South Pacific into the South Atlantic. For the O_1 constituent (**Plate 4b**), the energy flux is generally westward. Most of the energy approaching the tip of the Antarctic Peninsula from the southeast turns around the peninsula to continue westward along the Antarctic coast in the Bellingshausen Sea (**Plate 4b**). There is a small clockwise energy flux under the FRIS. At the continental shelf break in the southern Weddell Sea, the O_1 energy flux is very complicated. Diurnal energy on the southern shelf break has been previously characterized as being due to the large wave number mode of energetic, diurnally-forced, barotropic shelf waves [*Middleton et al.*, 1987]. There is, however, a strong correlation between the flux direction and the sequence of troughs along the southern slope (the gap between the peninsula and the General Belgrano Bank; the Ronne Depression; and the Filchner Depression). Our model appears to overpredict currents along the southern slope (see section 4.3.2, and *Padman et al.* [1998]). The diurnal tidal current along the southern slope will be considered in more detail in future model studies, but we believe that additional bathymetric information will be required before models can adequately describe ocean currents in this region.

5.2. *Energy Losses Due to Bottom Stress*

Tidal energy in the real ocean is dissipated by several mechanisms, including bottom friction, lateral friction, friction between the pack ice and the water, topographic drag, and flexure of the ice shelves. Our model parameterizes the first two of these sinks, however, the others are ignored. The time-averaged dissipation of energy per unit area by bottom friction, $\langle D_B(t) \rangle$, was evaluated as

$$\langle D_B \rangle = \rho_w C_D \langle |\mathbf{u}|^3 \rangle, \qquad \textbf{(6)}$$

where $\mathbf{u}$ is the barotropic velocity, and the angle brackets denote time averaging over the 45-day tidal analysis period of the model run.

Area-averaged and area-integrated values of $\langle D_B \rangle$ for 12 subregions of our model domain (**Figure 5**) are presented in **Table 5**. The highest average value, 0.067 W m^{-2}, occurs under FRIS and large values are also found for the slope in the southern Weddell Sea and the continental shelf subregions, except in the eastern Weddell Sea. Through the $|\mathbf{u}|^3$ dependence in (6), the actual distribution of $\langle D_B \rangle$ is clearly directly related to the spatial structure of u_{typ} (**Plate 3**). For example, most of the total energy loss for the FRIS

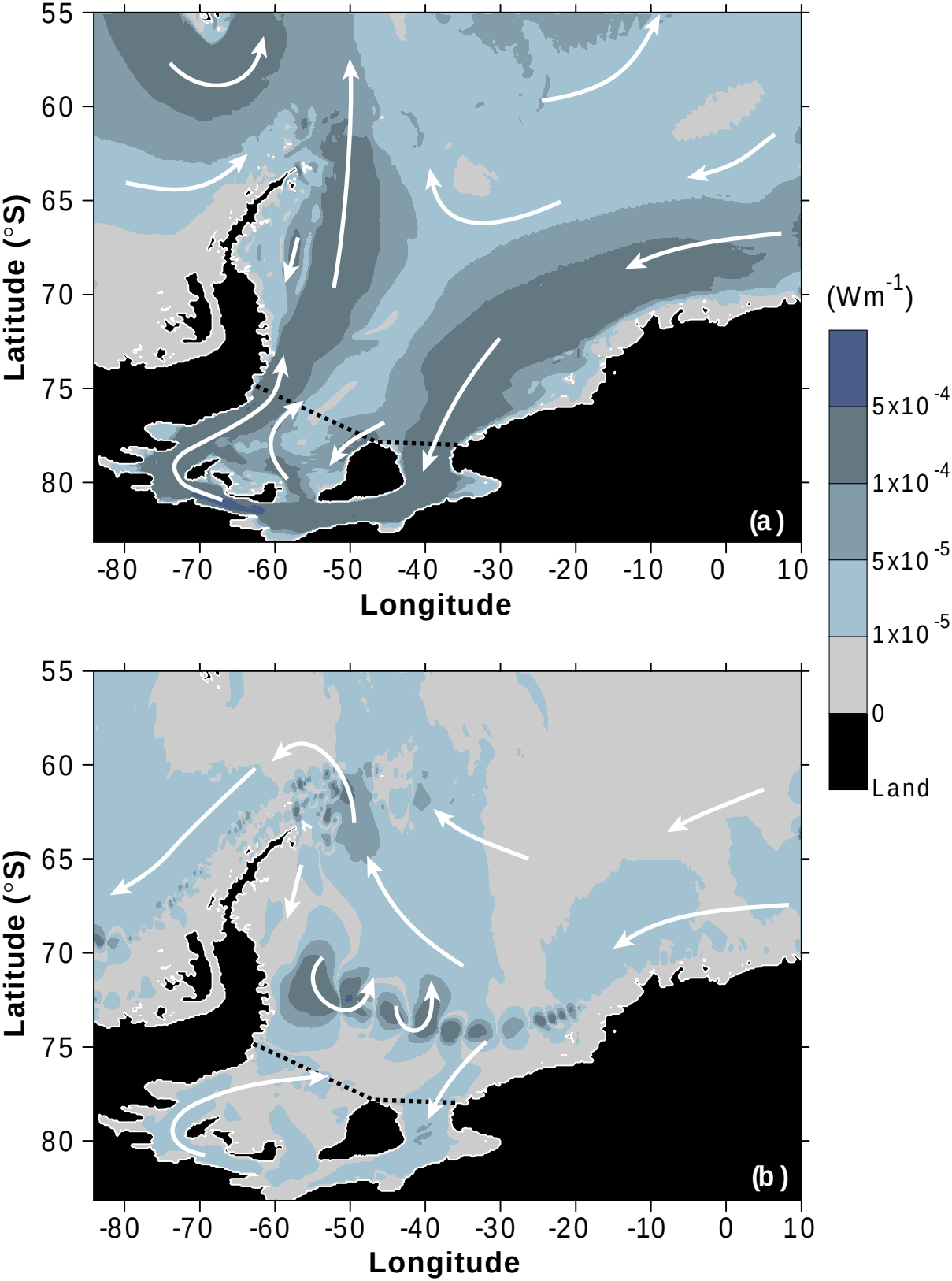
55
60
65
70
75
80
Latitude (°S)
-80
-70
-60
-50
-40
-30
-20
-10
0
10
Longitude
(a)
(b)
(Wm-1)
5x10-4
1x10-4
5x10-5
1x10-5
0
Land

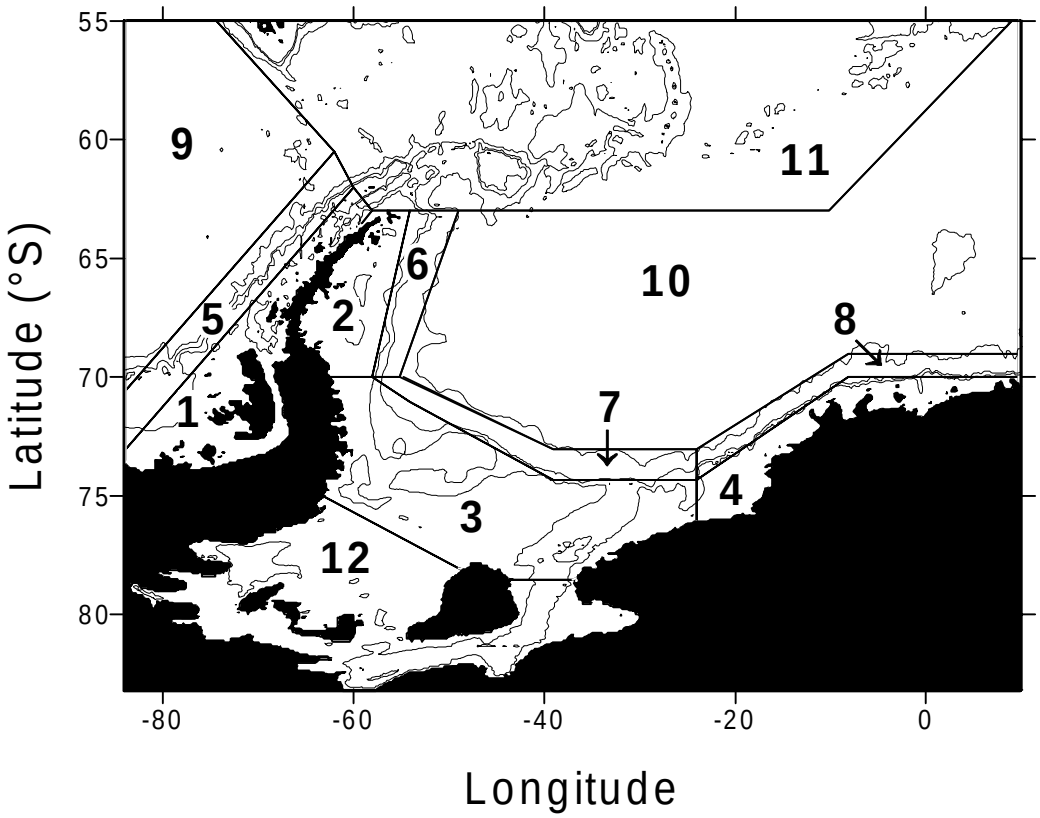

Fig. 5. Subregions for which area-averaged values of energy dissipation by bottom friction have been calculated (see Table 5). The 500 and 3000 m isobaths (or water column thickness isolines under the FRIS) are indicated.

TABLE 5. Area, integrated dissipation rate due to bottom friction, and mean dissipation rate per unit area, for specified sub-regions of the model domain.

Region	Area (10^6 km^2)	$\iint D_B(x,y)$ (GW)	$\langle D_B \rangle$ (10^{-3} W m^{-2})
Shelf			
S. Pacific (1)	0.34	6	18
W. Weddell (2)	0.21	2	9
S. Weddell (3)	0.51	32	63
E. Weddell (4)	0.18	3	17
Slope			
S. Pacific (5)	0.29	0.29	1.0
W. Weddell (6)	0.13	0.48	3.7
S. Weddell (7)	0.17	5.1	29
E. Weddell (8)	0.22	0.14	0.6
Deep			
S. Pacific (9)	1.17	0.05	0.04
Weddell (10)	2.74	0.10	0.03
Scotia (11)	3.49	10	2.8
FRIS (12)	0.40	27	67
Total	9.9	86	8.7
[Baroclinic tide generation]†	—	33	3.0

† The domain-averaged energy loss from the barotropic tides to the internal waves as determined following *Sjöberg and Stigebrandt* [1992] is also given.

(27 GW) occurs at the front of the Ronne Ice Shelf, and most of the energy loss for the continental shelf regions occurs in the high velocity region over the General Belgrano Bank. The energy lost to dissipation in the deep water of the Weddell Sea (region 10) is small, since velocities are small throughout this region. Although the deep basins (regions 9-11) cover most of the domain (~75%), they account for less than 12% of the total energy loss to bottom friction. Nearly all of this dissipation occurs in the Scotia Sea near the tip of the Antarctic Peninsula, and along the Scotia Ridge.

The total tidal energy lost to bottom friction in our 4-constituent model is about 86 GW, giving a domain-averaged value of $\langle D_B \rangle \approx 0.0087$ W m^{-2}. The flux divergence across the open boundaries of our model domain is approximately -32 GW (i.e., a net flux into the domain) for all 4 tidal constituents combined. The 54 GW difference is primarily due to local astronomical forcing (67 GW), with a small additional term due to lateral viscosity.

6. SOME IMPLICATIONS OF MODEL RESULTS

In this section we discuss two ways in which tidal currents can modify the general circulation and hydrography of the Weddell Sea. These are: the influence of tides on the effective friction experienced by the mean flow; and the generation of baroclinic tides and other internal gravity waves that can then lead to significantly higher effective diffusivities in the pycnocline. We also briefly review the implications of our model for estimates of the energy losses to ice shelf flexure. One of the most significant effects of tides in ice-covered seas, the distortion of the sea-ice cover, is discussed by *Padman et al.* [1998].

6.1. *Relationship Between Tides and Mean Currents*

The general circulation in the Weddell Sea is dominated by the Weddell Gyre, which flows clockwise [*Orsi et al.*, 1993]. The total volume transport of the gyre is about 30 Sv (1 Sv=10^6 m^{3}s^{-1}), which is concentrated in boundary currents on the southern and western sides of the basin [*Fahrbach et al.*, 1994]. A maximum mean speed of 16 cm s^{-1} has been reported in the Weddell coastal current, but 6 cm s^{-1} is a more typical value for the mean velocity over the shelf, and speeds less than 1 cm s^{-1} are typical for the deep basins [*Fahrbach et al.*, 1994].

Various studies have demonstrated that the tides can have a significant effect on the mean circulation, by generating residual currents and increasing the effective bottom friction felt by the mean flow. Generation of residual velocities has been described by *Loder* [1980], *Robinson* [1981], *Padman et al.* [1992], and *Kowalik and Proshutinsky* [1995], among others. While most of the processes responsible for residual currents will not be discussed here, we note that the necessary conditions for significant residual currents do exist within our model domain. Here, we only consider the role of tides in modifying the effective friction felt by the non-tidally-forced mean flow, which is driven primarily by wind stress and thermohaline forcing (air/sea and ice/ocean salt and heat exchanges). The increased effective friction due to the mean flow also affects tidal velocities. However, since tidal currents are usually much stronger (see below), they will have a more significant effect on the mean flow than the mean flow has upon them.

Mean currents along the southern and western margins of the Weddell Gyre were assumed to vary with water depth, from a maximum of 6 cm s^{-1} at the 500 m isobath (i.e., the continental shelf) to a minimum of 0.5 cm s^{-1} at the 3500 m isobath (following *Fahrbach et al.* [1994]). The ratio of the model typical tidal speed (u_{typ}: (3)) to the mean current $\langle |\mathbf{u}| \rangle$, was then determined at each location. Tidal currents generally exceed the mean currents in the Weddell Gyre. At the Ronne Ice Shelf edge and over the General Belgrano Bank, $u_{\mathrm{typ}}/\langle |\mathbf{u}| \rangle$ is about 5-10; over the continental shelf and slope, the ratio is 2-5.

The effect of the additional velocity variance from the tidal flows on the effective benthic friction felt by the subtidal, or "mean", currents can be estimated following *Noble et al.* [1983]. They noted that the bottom stress experienced by the subtidal flow can be written as

$$\tau_b = C_D(\mathbf{u}|\mathbf{u}|)_{\text{lowpass-filtered}} = C_E \mathbf{u}_s|\mathbf{u}_s|. \qquad \textbf{(7)}$$

Here, $\mathbf{u}$ is the total near-bottom current, and $\mathbf{u}_s$ is the subtidal current. When the tidal current amplitude, $|\mathbf{u}_{\mathrm{tide}}|$, is much larger than $|\mathbf{u}_s|$, the effective drag coefficient, C_E, is related to the bottom drag coefficient, C_D, by

$$C_E \approx \frac{|\mathbf{u}_{tide}|}{|\mathbf{u}_s|} C_D \,. \qquad \textbf{....(8)}$$

If the mean bottom velocity in the absence of tides ($\mathbf{u}_{\text{no tides}}$) is the velocity required for the bottom stress to balance the forcing (e.g., wind stress), then the mean velocity with tides included will be given by

$\mathbf{u}_s/\mathbf{u}_{no\ tides} \approx (C_D/C_E)^{1/2}$. That is, for our case of $|\mathbf{u}_{tide}|/|\mathbf{u}_s| \approx 2.5$, the mean flow with tides added is about 60-70% of the current in the absence of tides. In our ideal ocean, this is equivalent to reducing the gyre volume transport by the same fraction.

Gordon et al. [1981] estimated the mean circulation for the Weddell Basin to be 76 Sv, based on integrating the Sverdrup transport without bottom friction. A reduced estimate of 46 Sv was obtained by applying the model of *Bye and Veronis* [1979], where linear friction and the gyre "aspect ratio" are taken into account. This latter estimate is 1.5 times the 30 Sv obtained by *Fahrbach et al.* [1994] from current meter measurements. From our crude estimate and model (wind stress balances bottom friction), the inclusion of the tides in a circulation model would reduce the mean transport by a factor of about 1.5, thereby reconciling the value based on *Bye and Veronis* [1979] with *Fahrbach's* measurements. This simple approach cannot provide accurate Gyre transport values, but it is clear that the potential exists for tides to significantly modify the transport, and efforts should be made to include this influence in general circulation models. This could be easily achieved by using a spatially-dependent drag coefficient, $C_E(x,y)$ that has been evaluated following the analysis technique described above.

6.2. *Baroclinic Tide Generation*

Energy dissipation in our tidal model occurs primarily through bottom friction, with a smaller contribution from lateral viscosity. Other dissipative terms, such as stress at the base of the sea ice, have not been included in our model formulation. In a stratified ocean energy can also be lost from the barotropic tide by the generation of baroclinic tides and other internal gravity waves. While the baroclinic kinetic energy density may be small compared with the barotropic component, the velocity shear associated with baroclinic tides can be a major source of turbulent mixing in the Weddell Sea pycnocline [*Stanton et al.*, 1998].

Bell [1975] studied the generation of internal waves when currents flow over rough topography, and estimated an average energy loss from the barotropic tide of about 0.001 W m^{-2} (see also, *Polzin et al.* [1997]). *Sjöberg and Stigebrandt* [1992] estimated fluxes from the barotropic tide into the internal tide, using a model that calculated the baroclinic modes that are required to satisfy boundary conditions at bathymetry represented by steps. Their mean deep-ocean value was about 0.004 W m^{-2}. Some of this baroclinic energy can be made available to turbulent mixing in the pycnocline through non-linear processes such as wave-wave interactions. We would expect the strongest mixing to occur near regions of strongest generation. This is consistent with observations in the eastern Arctic Ocean, where higher kinetic energy dissipation in the pycnocline was linked to energetic tidal currents over the Yermak Plateau [*Padman et al.*, 1992; *Padman*, 1995]. A baroclinic model of the Arctic Ocean that included simple mixing parameterizations [*Polyakov*, 1995] found enhanced mixing over continental slopes, with resultant generation of near-surface mean geostrophic currents. Similarly, *Parsons* [1995] found that temperature differences over topographic features were consistent with enhanced mixing due to internal tides. In the Weddell Sea, baroclinic tides have been observed near Maud Rise [*Robertson et al.*, 1995b; *Stanton et al.*, 1998] and in the northwestern Weddell Sea by *Foster* [1994].

We used the formulation of *Sjöberg and Stigebrandt* [1992] to determine the energy loss to internal tides for our model domain (**Figure 6**). We assumed that the maximum buoyancy frequency was 3 cycles per hour, and that the scaling thickness (δ) for the permanent pycnocline was 50 m when the water depth was greater than 500 m. For water depths less than 500 m, δ was taken to be 10% of the water depth. Calculations were performed for both the M_2 and S_2 constituents, with the energy loss being summed for the first ten baroclinic modes. Since the diurnal constituents have frequencies that are much less than f, only the semidiurnal constituents can generate freely propagating baroclinic tides. The modeled energy loss to baroclinic tides was greater than 0.01 W m^{-2} for parts of the continental shelf/slope break, the front of the Ronne Ice Shelf, and much of the Bransfield Strait and elsewhere over the rough bathymetry of the Scotia Ridge (**Figure 6**). Energy losses exceeding 1 W m^{-2} are predicted in some small areas in the Bransfield Strait. Strong baroclinic tides are not predicted to be locally generated at either the AnzFlux (Antarctic Zone Flux Experiment) or *Foster* [1994] locations (marked "A" and "F" on **Figure 6**) where they have been observed. They could, however, be generated over nearby bathymetric features, such as the shelf edge and Maud Rise, then propagate to these locations. The domain-averaged energy loss is about 0.003 W m^{-2} for the M_2 and S_2 constituents combined.

It is interesting to speculate on the amount of mixing that might be generated in the pycnocline in response to baroclinic tide generation. Assume that,

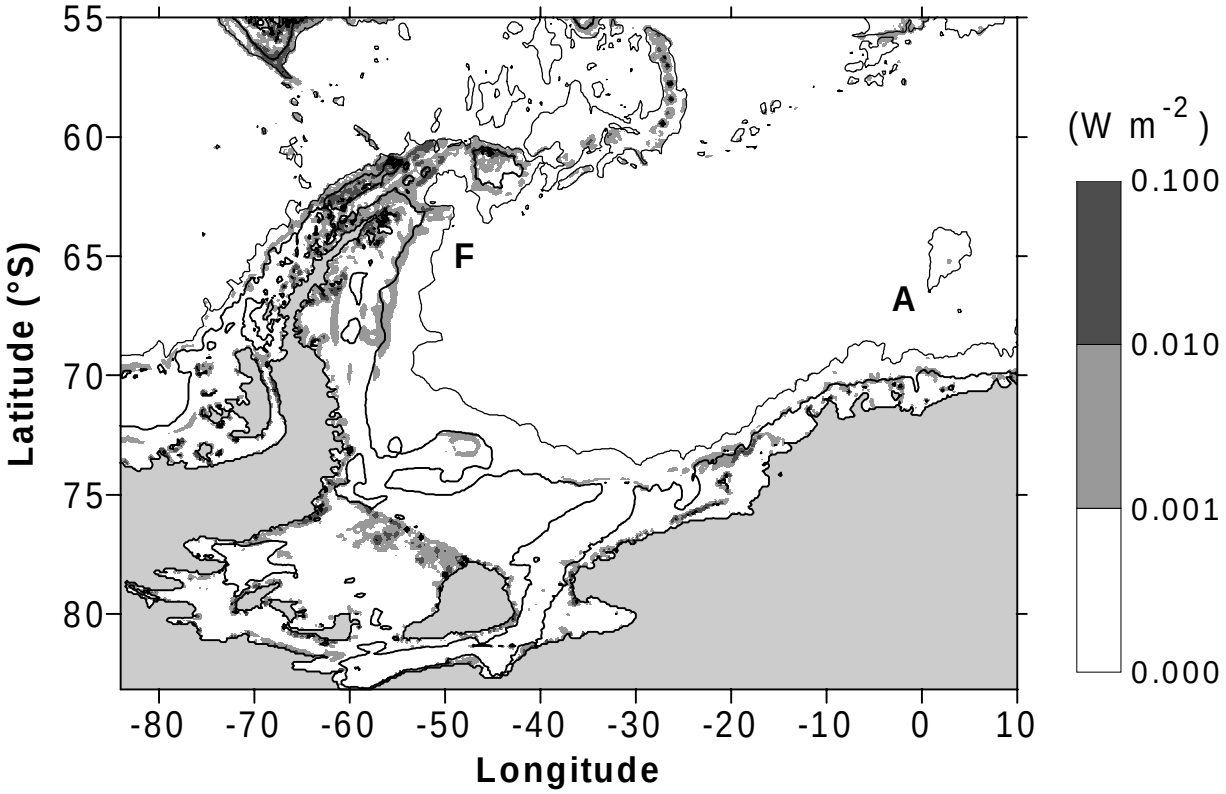

Fig. 6. The energy flux from barotropic tides to internal waves, following *Sjöberg and Stigebrandt* [1992]. The 500 and 3000 m isobaths (or water column thickness isolines under the FRIS) are shown. The location of the Anzflux baroclinic tide observation is denoted with an "A" and that of *Foster* [1994] with an "F".

through internal wave propagation, all the baroclinic energy is uniformly distributed in the model, and is also dissipated within the model domain at the same rate at which it is generated. If the 0.003 W m^{-2} mean production is balanced by uniform dissipation in a 100 m thick pycnocline ($H_{pyc}\approx 2\delta$), then the mean dissipation rate, $\langle\varepsilon\rangle$ is about 3×10^{-8} W kg^{-1}. Following *Osborn* [1980], we then estimate the vertical turbulent eddy diffusivity from $K_v=\Gamma\varepsilon/N^2$, where Γ is the "mixing efficiency", taken to be 0.2. For N=3 cph, we obtain $K_v\approx 2\times10^{-4}$ m^2 s^{-1}. If the mean temperature difference across the pycnocline is 2.5°C, i.e., $\langle\partial T/\partial z\rangle$=0.025°C m^{-1}, then the heat flux is $F_H=\rho c_p K_v\langle\partial T/\partial z\rangle\approx 25$ W m^{-2} (c_p is the specific heat capacity of seawater). This heat flux is the same order of magnitude as the average value required to balance the heat budget for the Weddell Sea [*Fahrbach et al*., 1994] and an order of magnitude higher than the diapycnal heat fluxes of 3 W m^{-2} estimated from observations in the western Weddell Sea [*Robertson et al*., 1995a]. There are many caveats to the above calculation, including the possibility that much of the generated baroclinic energy is actually dissipated close to the seabed [*Polzin et al*., 1997] rather than in the strongly-stratified pycnocline. Nevertheless, we believe that generation of baroclinic tides may play a significant role in the upward flux of WDW heat towards the ocean surface. Furthermore, Figure 6 identifies the regions where baroclinic tide generation is expected to be strongest: many of these areas are also important for larger-scale processes occurring in the Weddell Sea. For example, generation is high along the shelf break, where mixing at the shelf/slope front between shelf water types and WDW can lead to bottom water formation [*Foster et al*., 1987]. Generation is large in the Bransfield Strait and along the Scotia Ridge, where the water of the Antarctic Circumpolar Current interacts with Weddell Gyre water in the Weddell-Scotia Confluence. Generation is also strong at the FRIS front, suggesting a mechanism for mixing between the open shelf circulation and the dynamically isolated circulation under the ice shelves [*Grosfeld et al*., 1997]. From their model of circulation under ice shelves *Grosfeld et al*. suggest that very little advective transport occurs across the ice front (because of the strong cross-frontal gradient in f/H), thus isolating the ice-shelf circulation from the adjacent continental shelf. The energetic tides along the ice front suggest that strong cross-frontal mixing could occur in this region, reducing the isolation of these two flow regimes.

6.3. *Ice Shelf Energy Losses*

Early studies suggested that the interaction of tides with the glacial ice shelves surrounding Antarctica might be a major component of the total global tidal power dissipation of about 2500 GW [*Doake*, 1978]. The proposed dissipation mechanism, flexing of the glacial ice by spatial gradients in tidal elevation, is not included in our model. As we have shown above, however, our model predicts the tidal elevation field of the non-ice-shelf portion of the model domain quite well. Tidal energy fluxes must also, therefore, be reasonably well represented. In our model, a total of 66 GW of tidal energy enters the ice shelf cavity, and this is, therefore, approximately the maximum that can be lost by all dissipative processes under FRIS. Benthic and ice/water friction in our model accounts for about 27 GW. *Ray and Egbert* [1997] noted that most energy dissipated by the Antarctic ice shelves must first cross 60°S, since very little forcing of the dominant M_2 tide occurs south of this latitude. They used two different global tidal models to estimate an energy flux for the M_2 constituent of 1 and 42 GW northwards across the 60°S latitude line for all longitudes. In our regional model we find a total flux of about 63 GW northward across 60°S between 84°W and 10°E, with a similar pattern to *Ray and Egbert* [1997]. Hence, neither the global models nor our regional tidal model support the hypothesis of significant (in global terms) dissipation through ice shelf flexure. *Ray and Egbert* [1997] attributed *Doake*'s overestimation to the use of a few poor tidal observations and an incorrect model for the tidal energy absorbed by ice shelf flexure. *Vaughan* [1995] investigated the flexure of the ice shelves due to tides and reached a similar conclusion. Despite this result, the interaction of tides with ice shelves remains a potentially significant process [*Makinson and Nicholls*, 1996; *Smithson et al*., 1996].

7. CONCLUSIONS

We have developed a high-resolution barotropic model of tides in the Weddell Sea. The ocean cavity under the Filchner-Ronne Ice Shelf was explicitly included in the model domain. Four constituents were modeled, M_2, S_2, O_1, and K_1. Modeled tidal elevation amplitudes exceed 1 m at the back of the FRIS and the Larsen Ice Shelf. Modeled typical tidal speeds are greater than 0.1 m s^{-1} over most of the continental shelves. The highest speeds, greater than 75 cm s^{-1}, occur in the shallow water over the General Belgrano Bank and near the front of the Ronne Ice Shelf. Typical tidal currents over most of the Weddell Sea are 2-10 times greater than mean flows

associated with wind and thermohaline forcing. Tides therefore provide a significant fraction of the total oceanic kinetic energy, with a commensurately important influence on the oceanography of the region.

Most of the modeled tidal elevations agreed very well with available measurements, which include both tide gauges and satellite altimetry. Agreement between model predictions of major-axis currents and available measurements is less satisfactory, although still reasonable given the large potential errors that can be ascribed to inadequate bathymetric data. For the open ocean areas, standard deviations for the differences between modeled and measured tidal constituent elevations ranged from 2-5 cm in amplitude and up to 8° in phase. Similar comparisons against satellite altimetry data gave rms differences of 1-3 cm in amplitude. The major axis for the tidal velocity ellipses showed standard deviations of about 1 cm s^{-1} for deep-water regions, where tidal currents are small. Larger differences were seen for measurements under and near the Filchner/Ronne Ice Shelf. The elevation coefficients in this region had standard deviations of 8-14 cm in amplitude and 12-70° in phase when compared with tidal gauge data. For velocities under the ice shelf, the standard deviations of the major axis of the velocity ellipses ranged from 1.4 to 3.5 cm s^{-1}.

The tidal energy budget for our model is dominated by an energy influx through the eastern boundary, efflux through the northern and western boundaries, local astronomical forcing, and dissipation by bottom stress within the domain. The highest energy loss to bottom stress occurs in shallow regions with rapidly changing bathymetry, particularly under the ice shelves and on the continental slope. Mean energy losses in these areas are 0.009-0.067 W m^{-2}: the energy loss over the entire domain is 86 GW. We used the formulation of *Sjöberg and Stigebrandt* [1992] to estimate the potential in the real, stratified ocean for an additional loss of about 0.003 Wm^{-2} by generation of baroclinic tides (33 GW for the total model domain). This term is significantly smaller than the domain-integrated bottom frictional losses. Nevertheless, it may represent the largest single source of energy available to drive diapycnal mixing within the pycnocline. Spatial variability of pycnocline mixing rates could lead to significant geostrophic velocities in some areas.

Rough estimates for the increase in mean effective bottom stress due to the addition of tides with a quadratic bottom stress formulation ($\tau_b = C_D|\mathbf{u}|^2$) suggest that the mean gyre transport could be reduced by about 30% by incorporating tidal motion into general circulation models.

In the future, additional tidal constituents will be included in an effort to raise the total explained tidal variance. A dynamic/thermodynamic coupled ice model could be added to explore the influence of the ocean tides on the ice cover, and vice versa. With a realistic ice model, seasonal effects of the ice cover on the tides can then be investigated. For a similar model for the Arctic Ocean, *Kowalik and Proshutinsky* [1994] found that ocean tides can have a profound effect on the ice cover and the heat and salt exchanges at the air/ice/water interface, although the addition of sea ice to their tidal model had little influence on the ocean tides. The dissipation of energy due to the flexure of the ice shelves could also be parameterized in our model. While we have shown that the ice shelves are not a major sink of global tidal energy, there is a potential for significant modification to tidal predictions for the western Weddell Sea, since much of the tidal energy in this region has previously circulated under the Filchner/Ronne Ice Shelf. Baroclinic effects could be incorporated into the model by adding another dimension and including stratification. Additionally, as more data become available, "data assimilation" methods could be used to improve the model results.

These modifications should improve our understanding of the relationships between tides and other processes that have a direct bearing on topics of both regional and global significance. These processes include stability of the sea ice cover (therefore, the regional mean albedo and oceanic heat loss to the atmosphere), and stability of the ice shelves, which contribute to the global freshwater budget. However, the most fundamental limitation to our tidal model is the paucity of good bathymetric data, especially in the southwestern Weddell Sea. This limitation, which is highlighted by model sensitivity studies [*Padman et al*. 1998], is likely to apply also to regional, non-tidal models such as might be used to estimate Warm Deep Water and Ice Shelf Water production and their influence on AABW formation.

Appendix A: Review of Large Discrepancies Between the Model Elevations and the Measurements

The differences for the model elevation estimates greater than a cutoff of 25% will be examined below for each of the constituents. The largest discrepancies occurred with the *Thiel et al.* [1960] observations (77°42'S , 41°8'W). The model overestimates the M_2 and S_2 constituents by 20 cm (46%) and 23 cm (100%), respectively, and underestimates K_1 by 15 cm (-37%) (circled points in **Figures 4a, b & d**). The differences at this location are believed to be due to errors in the bathymetry or the location of the ice shelf. Although this location was on an ice shelf when the measurement was obtained, the present estimates do not show an ice shelf at this location. A significant difference was found at *Doake* [1992] site under the Ronne Ice Shelf (77°45'S, 64°30'W). Here the model underpredicts O_1 by 16 cm (-31%) (denoted with a square in **Figure 4c**). This measurement has a short record length (9 days). The short record length (20 days) at the *Lutjeharms et al.* [1985] site (70°12'S, 2°44'W) is probably the cause of the underestimates of 10 cm
(-26%) and 13 cm (-36%) for the S_2 and K_1 constituents at this site (denoted with squares in **Figures 4b and d**). The difference of 6 cm (26%) for S_2 at the *Hisdal* [1965] site (70°30'S, 2°32'W) is also due to its short record length of 3 days (denoted with a square in **Figure 4b**). The *Middleton et al.* site (74°28'S,37°39'W) was underestimated by the model by 13 cm (-36%) for the K_1 constituent. This underestimate may be measurement error or a result of continental shelf waves. The continental shelf/slope edge in this area generates continental shelf waves that amplify the diurnal constituents. The overestimate of 6 cm (50%) for K_1 at the *Smithson* [1992] site (60°51'S, 54°43'W) may result from the same mechanism.

Appendix B: Review of Large Discrepancies Between the Model Velocity Ellipse Major Axes and the Measurements

The largest differences occur at the *Foldvik et al.* [1982a] site with a short record length (4.2 days), where all constituents had large differences, 7.7 (351%), 4.2 (248%), 12.8 (152%), and 7.3 cm s^{-1} (47%) for the M_2, S_2, O_1, and K_1 constituents, respectively (denoted with squares in **Figures 4i-l**). Short record lengths may be responsible for the under-predictions at four of the *Levine et al.* [1997] sites (15 days). These points also have squares around them in **Figures 4j-l**. Bathymetric error probably accounts for errors in the S_2, O_1, and K_1 constituents at one of the *Fahrbach et al.* [1992;1994] sites near 71°3'S, 11°45'W. Bathymetric errors are also believed to be the source of the differences at the *Nygaard* [1995] site, where the model underpredicted the diurnal constituents by 4.6 (-55%) and 5.8 cm s^{-1} (-62%) for the O_1 and K_1 constituents, respectively (circled in **Figures 4k and l**). For this site, however, baroclinic effects are another possibility, since the base of the ice shelf is near 200 m depth and some differences were observed between the two meters on this mooring. This location is near the ice shelf edge and in an area where the bathymetry is not well known. One of the three long record length *Fahrbach et al.* [1992;1994] sites located near 71°3'S, 11°45'W shows a difference exceeding 25% for S_2, which has been attributed to bathymetric errors (circled in **Figure 4j**). However, measurement errors are also a possible cause since the differences are less than the uncertainties for two of the three locations. Bathymetric errors are the probable source for the differences in M_2, O_1, and K_1 at the *Middleton et al.* [1982] site near the edge of the Filchner Depression (74°40'S, 33°56'W) (circled in **Figures 4i, k, and l**) and the *Fahrbach et al.* [1992, 1994] site in a region of complicated bathymetry (63°30'S, 52°6'W) (circled in **Figure 4k**).

Of the remaining differences, the largest for M_2 occur for a group of sites near 74°S (the group of points below the uncertainty band in **Figure 4i**). The critical latitude, where the M_2 tidal frequency equals the inertial frequency, occurs at 74°28'30' S. Two of the four *Middleton et al.* [1987, 1982] and the *Foldvik et al.* [1990] locations near this critical latitude show differences greater than 2.0 cm s^{-1} (ranging from 40 to 111%). These discrepancies between the model predictions and the measurements may be a result of effects of the critical latitude. *Furevik and Foldvik* [1996] found that both the benthic boundary layer and water column turbulence were significantly increased near the critical latitude. These changes are neglected in the model where the drag parameterization is independent of the latitude and tidal frequency.

Five other points for the diurnal constituents lie significantly below the uncertainty band (**Figures 4k and l**). These are the *Middleton et al.* [1982, 1987] and *Foldvik et al.* [1990] measurements near 74°S and 37°-39°W. These discrepancies, along with those for four *Fahrbach* [1992, 1994] observations near 71°3'S, 11°45'W and a *Fahrbach et al.* [1992, 1994] observation further east on the continental shelf (70°26'S, 8°18'W), are believed to be associated with

inadequate model representation of continental shelf waves.

Acknowledgments. We are grateful to Ed Zaron for his assistance with the model and to Mark Abbott for providing the CM-5 Connection Machine computing resources. Lana Erofeeva carried out many of the energy budget calculations and model sensitivity studies. Eberhard Fahrbach and Keith Nicholls provided tidal analyses for their recent-acquired current meter data. We would also like to acknowledge the assistance of Robin Muench, Michael Smithson and Christoph Kottmeier. Ole Andersen and three anonymous reviewers provided valuable comments on the original manuscript. This work was funded by grants DPP-9024695 and OPP-9317319 from the National Science Foundation.

REFERENCES

Aanderaa Instruments, RCM4/5 Operating Manual, *Technical Publication No. 119*, Aanderaa Instruments, Bergen, Norway, 1979.

Andersen, O. B., New ocean tide models for loading computations, *Bull. Int. Mare Terr., 102*, 9256-9264, 1995.

Andersen, O. B., P. L. Woodworth, and R. A. Flather, Intercomparison of recent ocean tide models, *J. Geophys. Res., 100*, 25,261-25,282, 1995.

Barber, M., and D. Crane, Current flow in the northwest Weddell Sea, *Antarctic Science, 7*, 39-50, 1995.

Bell, T. H., Topographically generated internal waves in the open ocean, *J. Geophys. Res.*, 80, 320-327, 1975.

Bersch, M., G. A. Becker, H. Frey, and K. P. Koltermann, Topographic effects of the Maud Rise on the stratification and circulation of the Weddell Gyre, *Deep-Sea Res., 39*, 303-331, 1992.

Broecker, W. S., and T. H. Peng, *Tracers in the Sea*, Eldigio Press, Palisades, NY, 690 pp., 1982.

Bye, J. A. T., and G. Veronis, A correction to the Sverdrup transport, *J. Phys. Oceanog., 9*, 649-651, 1979.

Carmack, E. C., Water characteristics of the Southern Ocean south of the Polar Front, in *A Voyage of Discovery*, edited by M. Angel, pp. 15-41, Pergamon Press, Inc., Oxford, 1977.

Cartwright, D. E., and R. J. Taylor, New computations of the tide generating potential, *Geophys. J. R. Astron. Soc., 23*, 45-74, 1971.

Central Intelligence Agency, *World Data Bank, 2*, Central Intelligence Agency, Washington, D. C., 1972.

Doake, C. S. M., Dissipation of tidal energy by Antarctic ice shelves, *Nature, 275*, 304-305, 1978.

Doake, C. S. M., Gravimetric tidal measurements on Filchner Ronne Ice Shelf, in *Filchner-Ronne Ice Shelf Programme Report No. 6*, edited by H. Oerter, Alfred-Wegener Institute for Polar and Marine Research, Bremerhaven, Germany, 34-39, 1992.

Egbert, G. D., Tidal data inversion: interpolation and inference, *Progress in Oceanography* in press, 1997.

Egbert, G. D., A. F. Bennett, and M. G. G. Foreman, TOPEX/POSEIDON tides estimated using a global inverse model, *J. Geophys. Res., 99*, 24,821-24,852, 1994.

Eckstaller, A., and H. Miller, Gezeiten-Vertikalbewegung des Filchner Schelfeises (Tides and vertical movement of the Filchner Ice Shelf), *Ber. Polarforsch., 19*, 82-97, 1984.

Fahrbach, E., G. Rohardt, and G. Krause, The Antarctic coastal current in the southeastern Weddell Sea, *Polar Biology, 12*, 171-182, 1992.

Fahrbach, E., G. Rohardt, M. Schröder, and V. Strass, Transport and structure of the Weddell Gyre, *Ann. Geophysicae, 12*, 840-855, 1994.

Ffield, A., and A. L. Gordon, Tidal mixing signatures in the Indonesian Seas, *J. Phys. Oceanogr., 26*, 1924-1937, 1996.

Foldvik, A., and T. Kvinge, Bottom currents in the Weddell Sea, *Rep. No. 37*, 43 pp., University of Bergen, Bergen, Norway, 1974.

Foldvik, A., and T. Gammelsrød, Notes on southern ocean hydrography, sea-ice and bottom water formation, *Palaeogeog., Palaeoclim., and Palaeoecol., 67*, 3-17, 1988.

Foldvik, A., T. Gammelsrød, N. Slotsvik, and T. Tørresen, Oceanographic conditions on the Weddell Sea shelf during the German Antarctic Expedition 1979/80, *Polar Res., 3*, 209-226, 1982a.

Foldvik, A., T. Gammelsrød and T. Tørresen, Physical oceanographic studies in the Weddell Sea shelf during the Norwegian Antarctic Research Expedition 1978/79, *Polar Res., 3*, 195-207, 1982b.

Foldvik, A., T. Gammelsrød and T. Tørresen, Circulation and water masses in the southern Weddell Sea shelf, in *Oceanology of the Antarctic Continental Shelf, Antarc. Res. Series, 43*, edited by S. S. Jacobs, 5-20, AGU, Washington, D. C., 1985a.

Foldvik, A., T. Kvinge, and T. Tørresen, Bottom currents near the continental shelf break in the Weddell Sea, in *Oceanology of the Antarctic Continental Shelf, Antarc. Res. Series, 43*, edited by S. S. Jacobs, 21-34, AGU, Washington, D. C., 1985b.

Foldvik, A., J. H. Middleton, and T. D. Foster, The tides of the southern Weddell Sea, *Deep-Sea Res., 37*, 1345-1362, 1990.

Foreman, M. G. G., *Manual for tidal current analysis and prediction*, Pacific Marine Science Report No. 78-6, Institute of Ocean Sciences, Patricia Bay, Sidney, B.C., 70 pp., 1978.

Foster, T. D., Large, steplike temperature and salinity structures observed in the central Weddell Sea, , *Antarct. J., 29*, 99-100, 1994.

Foster, T. D., A. Foldvik, and J. H. Middleton, Mixing and bottom water formation in the shelf break region of the southern Weddell Sea, *Deep-Sea Res., 34*, 1771-1794, 1987.

Furevik, T., and A. Foldvik, Stability at M_2 critical latitude in the Barents Sea, *J. Geophys. Res., 101*, 8823-8837, 1996.

Gallagher, B. S., and W. H. Munk, Tides in Shallow Water: Spectroscopy, *Tellus, 23*, 346-363, 1971.

Gammelsrød, T., A. Foldvik, O. A. Nøst, Ø. Skagseth, L. G. Anderson, E. Fogelqvist, K. Olsson, T. Tanhua, E. P. Jones, and S. Østerhus, Distribution of water masses on the continental shelf in the southern Weddell Sea, in *The Polar Oceans and Their Role in Shaping the Global Environment*, Geophysical Monograph 85, AGU, Washington, D.C., p. 159-176, 1994.

Genco, M. L., F. Lyard, and C. Le Provost, The oceanic tides in the South Atlantic Ocean, *Ann. Geophysicae, 12*, 868-886, 1994.

Gordon, A. L., D. G. Martinson, and M. W. Taylor, The wind driven circulation in the Weddell-Enderby Basin, *Deep-Sea Res., 28A*, 151-163, 1981.

Grosfeld, K., R. Gerdes, and J. Determann, Thermohaline circulation and interaction between ice shelf cavities and the adjacent open ocean, *J. Geophys. Res., 203*, 15,595-15,610, 1997.

Haltiner G. J., and R. T. Williams, *Numerical Prediction and Dynamic Meteorology*, John Wiley and Sons, Inc., New York, 477 pp., 1980.

Hatayama, T., T. Awaji, and K. Akitomo, Tidal currents in the Indonesian Seas and their effect on transport and mixing, *J. Geophys. Res., 101*, 12,353-12,373, 1996.

Hisdal, V., On the tides at Norway Station, and adjacent coastal areas of Antarctica, Norwegian Antarctic Expedition, 1956-60, *Sci. Res., 9*, 21 pp, Norwegian Polar Institute, Oslo, 1965.

Jet Propulsion Laboratory, A collection of ocean tide models on CD-ROM, CD-ROM distributed by the *Jet Propulsion Laboratory*, Pasadena, California, 1996.

Kowalik, Z., and A. Y. Proshutinsky, The Arctic Ocean Tides, in *The Polar Oceans and Their Role in Shaping the Global Environment*, Geophysical Monograph 85, edited by O. M. Johannessen, R. D. Muench, and J. E. Overland, pp. 137-158, AGU, Washington, D. C., 1994.

Kowalik, Z., and A. Y. Proshutinsky, Topographic enhancement of tidal motion in the western Barents Sea, *J. Geophys. Res., 100*, 2613-2637, 1995.

LaBrecque, J. L., and M. E. Ghidella, Estimates of bathymetry, depth to magnetic basement, and sediment thickness for the western Weddell Basin, *Antarc. J. U. S., 27*, 68-70, 1993.

Le Provost, C., M. L. Genco, F. Lyard, P. Vincent, and P. Canceil, Spectroscopy of the world ocean tides from a finite element hydrodynamic model, *J. Geophys. Res., 99*, 24,777-24,797, 1994.

Levine, M. D., L. Padman, R. D. Muench, and J. H. Morison, Internal waves and tides in the western Weddell Sea: observations from Ice Station Weddell, *J. Geophys. Res, 102*, 1073-1089, 1997.

Loder, J.W., Topographic rectification of tidal currents on the sides of Georges Bank, *J. Phys. Oceanogr., 10*, 1399-1416, 1980.

Lutjeharms, J. R. E., C. C. Stavropolous, and K. P. Koltermann, Tidal measurements along the Antarctic coastline, in *Oceanology of the Antarctic Continental Shelf, Antarc. Res. Series, 43*, edited by S. S. Jacobs, pp. 273-289, AGU, Washington, D. C., 1985.

MacAyeal, D. R., Numerical simulations of the Ross Sea Tides, *J. Geophys. Res, 89*, 607-615, 1984.

Makinson, K., and K. W. Nicholls, Modeling tidal currents beneath Filchner-Ronne Ice Shelf, *Filchner-Ronne Ice Shelf Programme, Report 10*, 58-67, 1996.

Middleton, J. H., and T. D. Foster, Tidal currents in the central Weddell Sea, *Deep-Sea Res., 24*, 1195-1202, 1977.

Middleton, J. H., T. D. Foster, and A. Foldvik, Low-frequency currents and continental shelf waves in the southern Weddell Sea, *J. Phys. Oceanogr., 12*, 618-634, 1982.

Middleton, J. H., T. D. Foster, and A. Foldvik, Diurnal shelf waves in the southern Weddell Sea, *J. Phys. Oceanogr., 17*, 784-791, 1987.

National Geophysical Data Center, GEODAS CD-ROM worldwide marine geophysical data, *Data Announce. 92-MGG-02*, Natl. Oceanic and Atmos. Admin. U.S. Dep. Commer., Boulder, Colo., 1992.

Noble, M., B. Butman, and E. Williams, On the longshelf structure and dynamics of subtidal currents on the eastern United States continental shelf, *J. Phys. Oceanogr., 13*, 2125-2147, 1983.

Nygaard, E., Preliminary results from current measurements in position R2 (76°29' S, 53°00' W) outside the Ronne Ice Shelf in the southern Weddell Sea 1993-1994, unpublished report, Geophysical Institute, Bergen, Norway, 25 pp., 1995.

Orsi, A. H., W. D. Nowlin, Jr., and J. Whitworth III, On the circulation and stratification of the Weddell Gyre, *Deep Sea Res., 40*, 169-203, 1993.

Osborn, T.R., Estimates of the local rate of vertical diffusion from dissipation measurements, *J. Phys. Oceanogr., 10*, 83-89, 1980.

Padman, L., Small-scale physical processes in the Arctic Ocean, in *Arctic Oceanography: Marginal Ice Zones and Continental Shelves, Coastal and Estuarine Studies, 49*, edited by W. O. Smith and J. M. Grebmeier, pp. 97-129, AGU, Washington, D.C., 1995.

Padman, L., A. J. Plueddemann, R. D. Muench, and R. Pinkel, Diurnal tides near the Yermak Plateau, *J. Geophys. Res, 97*, 12,639-12,652, 1992.

Padman, L., C. H. Kottmeier, and R. Robertson, Tidal ice motion in the Weddell Sea, submitted to *J. Geophys. Res.*, 1998.

Parker, B. B., *Tidal Hydrodynamics*, 883 pp., John Wiley and Sons, New York, 1991.

Parsons, A. R., On the Barents Sea polar front in summer and interpretations of the associated regional oceanography using an Arctic Ocean general circulation model, Ph.D. thesis, 178 pp., Naval Postgraduate School at Monterey, September 1995.

Pedley, M., J. G. Paren, and J. R. Potter, The tidal spectrum underneath Antarctic Ice Shelves, *J. Geophys. Res.*, *91*, 13,001-13,009, 1986.

Polyakov, I.V., Maintenance of the Arctic Ocean large-scale baroclinic structure by the M2 tide, *Polar Research*, *13*, 219-232, 1995.

Polzin, K. L., J. M. Toole, J. R. Ledwell, and R. W. Schmitt, Spatial variability of turbulent mixing in the abyssal ocean, *Science*, *276*, 93-96, 1997.

Pond, S., and G. L. Pickard, *Introductory Dynamical Oceanography*, Butterworth-Heinemann Ltd., Oxford, England, 329 pp., 1978.

Potter, J. R., J. G. Paren, and M. Pedley, Tidal behaviour under an Antarctic ice shelf, *Br. Antarc. Survey Bull.*, *68*, 1-18, 1985.

Pratt, J. G. D., Tides at Shackleton, Weddell Sea, Trans-Antarctic Expedition, 1955-1958, *Sci. Rep. 4*, 21 pp., American Philosophical Society, Philadelphia, 1960.

Ramming, H. G., and Z. Kowalik, *Numerical Modeling of Marine Hydrodynamic: Applications to Dynamic Physical Processes*, Elsevier Oceanography Series, *26*, 368 pp., Elsevier Scientific Publishing Co., Amsterdam, 1980.

Ray, R. D., and G. D. Egbert, The flux of tidal power across latitude 60°S, *Geophys. Res. Let.*, *24*, 543-546, 1997.

Robinson, I. S., Tidal vorticity and residual circulation, *Deep-Sea Res.*, *28A*, 195-212, 1981.

Robertson, R. A., L. Padman, and M. D. Levine, Fine structure, microstructure, and vertical mixing processes in the upper ocean in the western Weddell Sea, *J. Geophys. Res.*, *100*, 18,517-18,535, 1995a.

Robertson, R. A., L. Padman, M. D. Levine, R. D. Muench, and M. G. McPhee, Internal waves in the eastern Weddell Sea during AnzFlux, IAPSO XXI General Assembly, Honolulu, HI, 1995b.

Schwiderski, E. W., Ocean tides, I, Global ocean tidal equations, *Mar. Geod.*, *3*, 161-217, 1980.

Sjöberg, B., and A. Stigebrandt, Computations of the geographical distribution of the energy flux to mixing processes via internal tides and the associated vertical circulation in the ocean, *Deep-Sea Res.*, *39*, 269-291, 1992.

Smith, A. M., The use of tiltmeters to study the dynamics of Antarctic ice-shelf grounding lines, *J. Glaciol.*, *37*, 51-58, 1991.

Smith, W. H. F., On the accuracy of digital bathymetric data, *J. Geophys. Res*, *98*, 9591-9603, 1993.

Smithson, M. J., Pelagic tidal constants 3, *IAPSO Publication Scientifique No.35*, 191 pp., 1992.

Smithson, M. J., A. V. Robinson, and R. A. Flather, Ocean tides under the Filchner-Ronne Ice Shelf, Antarctica, *Annals of Glaciology*, *23*, 217-225, 1996.

Stanton, T. P., L. Padman, and R. A. Robertson, Heat fluxes through the permanent pycnocline in the eastern Weddell Sea, submitted to *J. Geophys. Res.*, 1998.

Stephenson, S. N., C. S. M. Doake, and J. A. C. Horsfall, Tidal flexure of ice shelves measured by tiltmeter, *Nature*, *282*, 496-497, 1979.

Thiel, E., A. P. Crary, R. A. Haubrich, and J. C. Behrendt, Gravimetric determination of ocean tide, Weddell and Ross Seas, Antarctica, *J. Geophys. Res.*, *65*, 629-636, 1960.

Vaughan, D. G., Tidal flexure at ice shelf margins, *J. Geophys. Res.*, *100*, 6213-6224, 1995.

Vaughan, D. G., J. Sievers, C. S. M. Doake, G. Grikurov, H. Hinze, V. S. Pozdeev, H. Sandhäger, H. W. Schenke, A. Solheim, and F. Thyssen, Map of the subglacial and seabed topography; Filchner-Ronne-Schelfeis/ Weddell Sea, Antarktis, scale 1:2,000,000, *Institut für Angewandte Geodäsie*, Frankfurt am Main, Germany, 1994.

Viehoff, T., and A. Li, Iceberg observations and estimation of submarine ridges in the western Weddell Sea, *Int. J. Remote Sensing*, *16*, 3391-3408, 1995.

G. D. Egbert, 104 Ocean Admin Bldg, Oregon State University, Corvallis, OR 97331-5503,
(email: egbert@oce.orst.edu)

L. Padman, Earth and Space Research, 1910 Fairview Ave, East, Suite 102, Seattle, WA, 98102-3620,
(email: padman@esr.org)

R. Robertson, 104 Ocean Admin Bldg, Oregon State University, Corvallis, OR 97331-5503
(email: rroberts@oce.orst.edu)

(Received February 9, 1997; accepted August 13, 1997).